SCIENCE CHINA
Earth Sciences

•RESEARCH PAPER•

April 2020 Vol.63 No.4: 512–532
https://doi.org/10.1007/s11430-019-9567-y

Spatio-temporal variation in rock exhumation linked to large-scale shear zones in the southeastern Tibetan Plateau

Yukui GE[1], Jing LIU-ZENG[2*], Jinyu ZHANG[1], Wei WANG[1], Yuntao TIAN[3], Matthew FOX[4], Lingsen ZENG[5], Xiaoming SHEN[6], Heng WANG[1], Ze SU[6] & Kejia XIE[7]

[1] *State Key Laboratory of Earthquake Dynamics, Institute of Geology, China Earthquake Administration, Beijing 100029, China;*
[2] *Institute of Surface-Earth System Science, Tianjin University, Tianjin 300072, China;*
[3] *Guangdong Provincial Key Laboratory of Geodynamics and Geohazards, School of Earth Sciences and Engineering, Sun Yat-sen University, Guangzhou 510275, China;*
[4] *Department of Earth Sciences, University College London, Gower St., Kings Cross London, WC1E 6BT, UK;*
[5] *Key Laboratory of Deep-Earth Dynamics, Ministry of Natural Resources, Institute of Geology, Chinese Academy of Geological Sciences, Beijing 100037, China;*
[6] *Key Laboratory of Crustal Dynamics, Institute of Crustal Dynamics, China Earthquake Administration, Beijing 100085, China;*
[7] *Henan Province Non-ferrous Metals Geological Mineral Resources Bureau, Zhengzhou 450016, China*

Received July 26, 2019; revised November 10, 2019; accepted December 19, 2019; published online February 24, 2020

Abstract Crustal-scale shear zones are believed to have played an important role in the tectonic and landscape evolution of orogens. However, the variation of long-term rock exhumation between the interior of shear zones and adjacent regions has not been documented in detail. In this study, we obtained new zircon U-Pb, biotite $^{40}Ar/^{39}Ar$, zircon and apatite (U-Th)/He data, and conducted inverse thermal history modeling from two age-elevation profiles (the Pianma and Tu'er profiles) in the southeastern Tibetan Plateau. Our goal is to constrain the exhumation history of the Gaoligong and Chongshan shear zones and adjacent regions, so as to explore the effect of the shear zones on exhumation and their thermal effect on cooling that should not be ignored. Our results suggest that during the interval of 18–11 Ma the exhumation rates of rocks within the Gaoligong shear zone are anomalously high compared with those outside of. The rapid cooling during 18–11 Ma appears to be restricted to the shear zone, likely due to localized thermal effects of shearing and exhumation. After 11 Ma, both the areas within and outside of the shear zones experienced a similar two-stage exhumation history: slower cooling until the early Pliocene, and then a rapid increase in cooling rate since the early Pliocene. Our results indicate a synchronized exhumation but with spatially varied exhumation rates. Our study also highlights the important role of large-scale shear zones in exposing rocks, and thus the importance of the structural context when interpreting thermochronological data in the southeastern margin of the Tibetan Plateau.

Keywords Southeastern Tibetan Plateau, Exhumation, (U-Th)/He, Low-temperature thermochronometry, Shear zone

Citation: Ge Y, Liu-Zeng J, Zhang J, Wang W, Tian Y, Fox M, Zeng L, Shen X, Wang H, Su Z, Xie K. 2020. Spatio-temporal variation in rock exhumation linked to large-scale shear zones in the southeastern Tibetan Plateau. Science China Earth Sciences, 63: 512–532, https://doi.org/10.1007/s11430-019-9567-y

1. Introduction

The geomorphology of the southeastern margin of the Tibetan Plateau is characterized by relatively low relief upland which is being deeply incised by large rivers (the Yangtze, Langcang-Mekong, and Nu Jiang-Salween rivers, from east to west) (Fielding et al., 1994; Brookfield, 1998; Hallet and Molnar, 2001; Clark et al., 2005, 2006; Liu-Zeng et al., 2008;

* Corresponding author (email: earofwood@yahoo.com)

Royden et al., 2008; Zhang et al., 2018). Tectonically, the region is dominated by large-scale strike-slip fault and shear zone systems (Figures 1 and 2; e.g., Schärer et al., 1990; Leloup et al., 1993, 1995; Wang and Burchfiel, 1997; Zhang et al., 2011; Burchfiel and Chen, 2013; Wang et al., 2018). The Ailao Shan-Red River shear zone (ALS-RRSZ), the Chongshan shear zone (CSSZ), and the Gaoligong shear zone (GLSZ) are all hundred-kilometer-long continental-scale shear zones, which are also geomorphically prominent in the region (Tapponnier et al., 1990; Leloup et al., 1993; Molnar et al., 1993; Jolivet et al., 2001; Zhang et al., 2009; Burchfiel and Chen, 2013; Xu et al., 2015). The southeastern Tibetan Plateau is thus a natural laboratory for examining the role of tectonics in shaping the landscape.

Exhumation is increasingly recognized as a key process recording the long-term evolution of orogenic belts (e.g., Dahlen and Suppe, 1988; Arne et al., 1997; Leloup et al., 2001). Low-temperature thermochronological data provide important constraints on the timing and rate of exhumation, potentially enabling the resolution of controversies concerning the timing of regional surface uplift, exhumation, incision and deformation (Wolf et al., 1996; Moore and England, 2001; Reiners and Brandon, 2006; Blackburn et al., 2018). The southeastern Tibetan Plateau is especially important for examining the interaction between exhumation rate and crustal deformation or tectonically-driven rock uplift. Several low-temperature thermochronometric studies have been carried out in the region, in order to constrain the timing of bedrock cooling and exhumation rates (Tapponnier et al., 1990; Clark et al., 2005, 2006; Liu-Zeng et al., 2008, 2018; Wang et al., 2012; Shen et al., 2016; Yang et al., 2016; Wang et al., 2017; Tian et al., 2018; Wang et al., 2018).

In structurally active areas, the relationship between exhumation and crustal deformation is of key importance for understanding the evolution of the topography. The variation of long-term rock exhumation between shear zones and the adjacent regions has not been documented in detail, but it is important for evaluating whether the low-temperature ther-

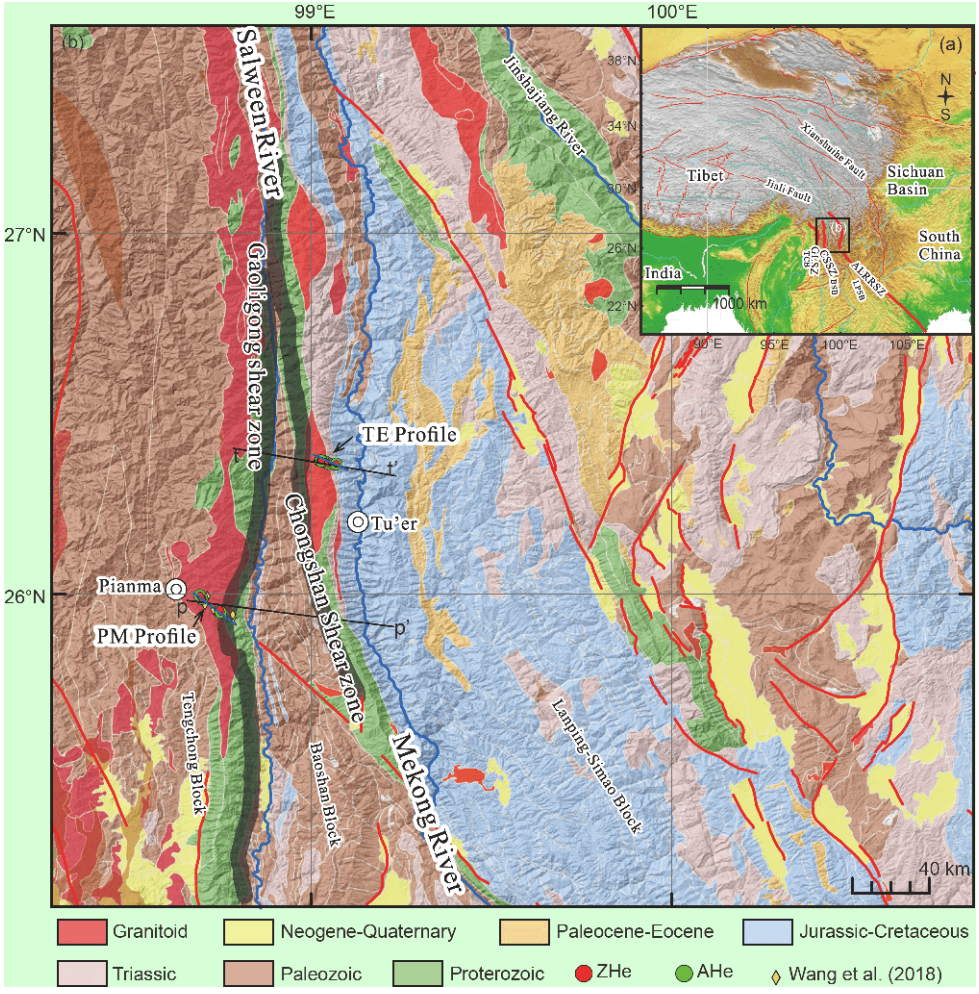

Figure 1 Simplified geological map of the Southeastern Tibetan Plateau, superimposed on shaded relief. Inset (a) is a DEM map of Tibet and southeastern Tibetan Plateau. Black frame on map in inset shows location of Figure 1 (b). Sample locations of this study are shown by circles. Lines p-p' and t-t' indicate cross-section locations presented in Figures 3 and 4, respectively.

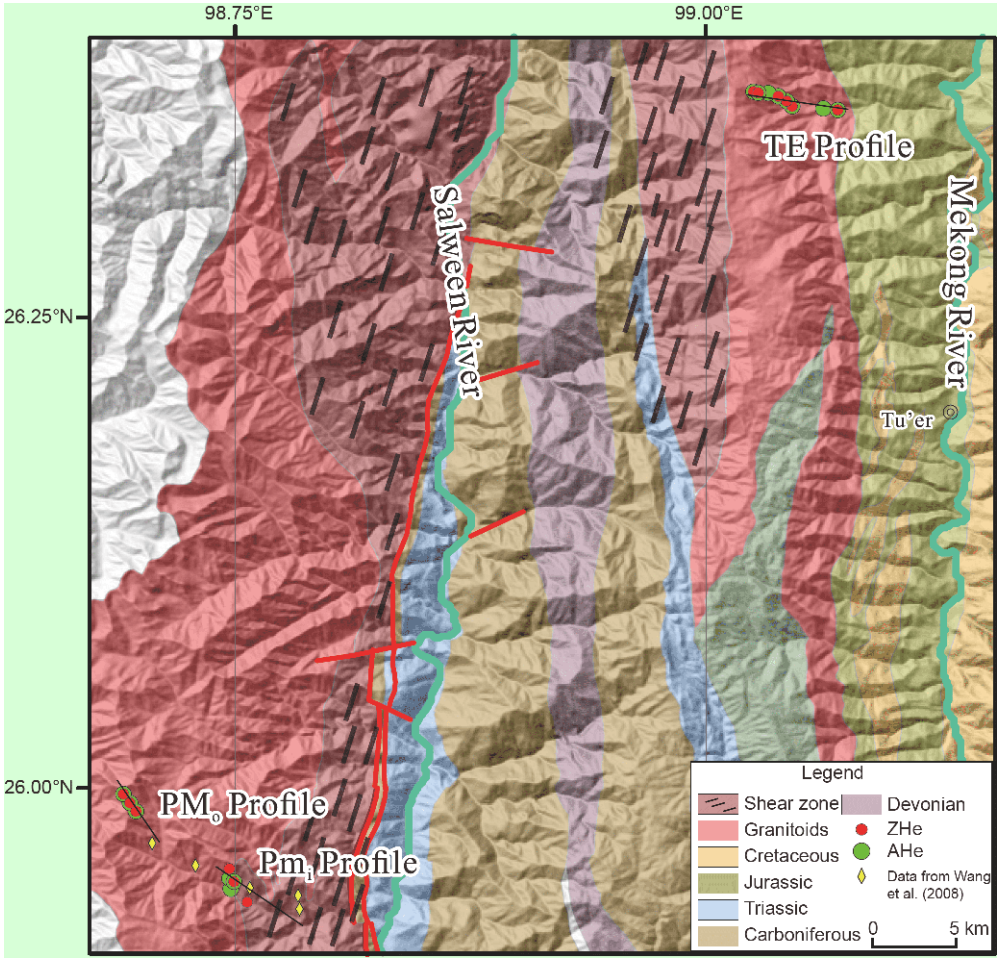

Figure 2 Geological map of the study area (modified after Bureau of Geology and Mineral Resources of Yunnan Province, 1990). Circles with red filling are the ZHe samples; circles with green filling are the AHe samples; diamond with yellow filling are the samples from Wang et al. (2018).

mochronological data reflect the actual cooling due to exhumation or the thermal effect of localized shearing. If there is a significant difference in exhumation rate between inside and outside the shear zone, an extrapolation of the data from samples within the shear zones to a region may lead to a misinterpretation of the evolution of regional exhumation. However, assessment of the relative influence of these factors requires the collection more data from a variety of different structural and geomorphic settings.

In order to learn more about the evolution of shearing and its effect on exhumation, we conduct low-temperature thermochronological investigation and adjacent to shear zones in the southeastern Tibetan Plateau. We collected 18 samples from two nearly vertical profiles along the Nu Jiang-Salween River, near Pianma (the Pianma profile) and the Langcang-Mekong River near Tu'er (the Tu'er profile) (Figures 3 and 4). The Pianma profile (PM profile) crosscuts the Gaoligong shear zone and focuses on structures both within and outside the shear zone, while the Tu'er profile (TE profile) is located to the east of the Chongshan shear zone. We present new zircon U-Pb data, biotite $^{40}Ar/^{39}Ar$ data, and zircon and apatite (U-Th)/He data, which provide constraints on the tectonic and erosional evolution of the shear zone and adjacent regions in the southeastern Tibetan Plateau. Our study reveals a spatio-temporal correlation between strike-slip faulting and exhumation.

2. Geological setting

The southeastern Tibetan Plateau is characterized by prominent, Cenozoic shear zones and faults (Zhong et al., 1990; Leloup et al., 1995; Morley, 2007; Zhang et al., 2010; Burchfiel and Chen, 2013; Xu et al., 2015). The near N-S-striking Gaoligong and Chongshan shear zones are two major large-scale shear zones which play an important role in the accommodation of intracontinental deformation (Akciz, 2004; Akciz et al., 2008; Zhang et al., 2011; Eroğlu et al., 2013). From west to the east, they divide the southeastern Tibetan Plateau into the Tengchong Block (TCB), the Baoshan Block (BSB) and the Lanping-Simao Block (LPSB) (Zhong et al., 1990; Akciz et al., 2008; Xu et al., 2015).

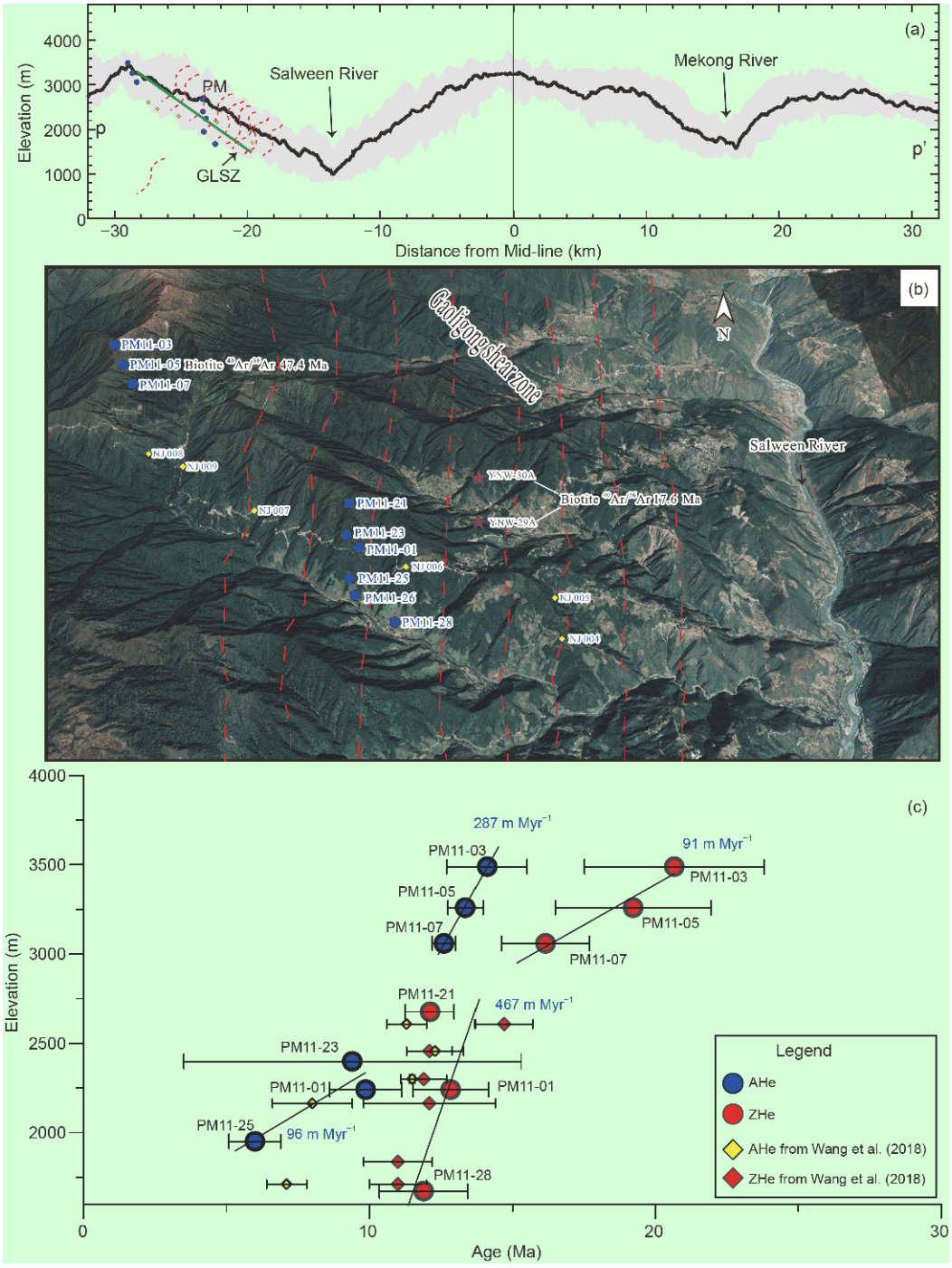

Figure 3 (a) Sample location on topographic swath profile. The swath profile p-p' shows the max, min and average topography, deep incision of major rivers, and the projected position of our samples. Circles are our new samples; diamond with yellow filling are the samples from Wang et al. (2018). (b) The GLSZ location and sample locations are shown on the Google Earth image. (c) Plots of zircon and apatite (U-Th)/He ages against elevation and the exhumation rates according the age-elevation relationship for PM profile.

Geological mapping has demonstrated that the Gaoligong shear zone and Chongshan shear zone are not belts of Precambrian-age metamorphic basement rocks (Bureau of Geology and Mineral Resources of Yunnan Province, 1990), but rather they are Cenozoic amphibolite grade gneisses with mylonitic structures and right- and left-lateral shear sense indicators (Akciz, 2004; Zhang et al., 2011, 2012a).

The Gaoligong shear zone is a narrow N-S-trending belt, 10-km wide and 600-km long, which is completely exposed along the Gaoligong Mountains west of the Nu Jiang-Salween River valley (Wang et al., 2008; Zhang et al., 2012a). It extends eastward and southward from the eastern Himalayan syntaxis, forming the boundary between the Tengchong and Baoshan blocks (Zhong et al., 1990; Wang

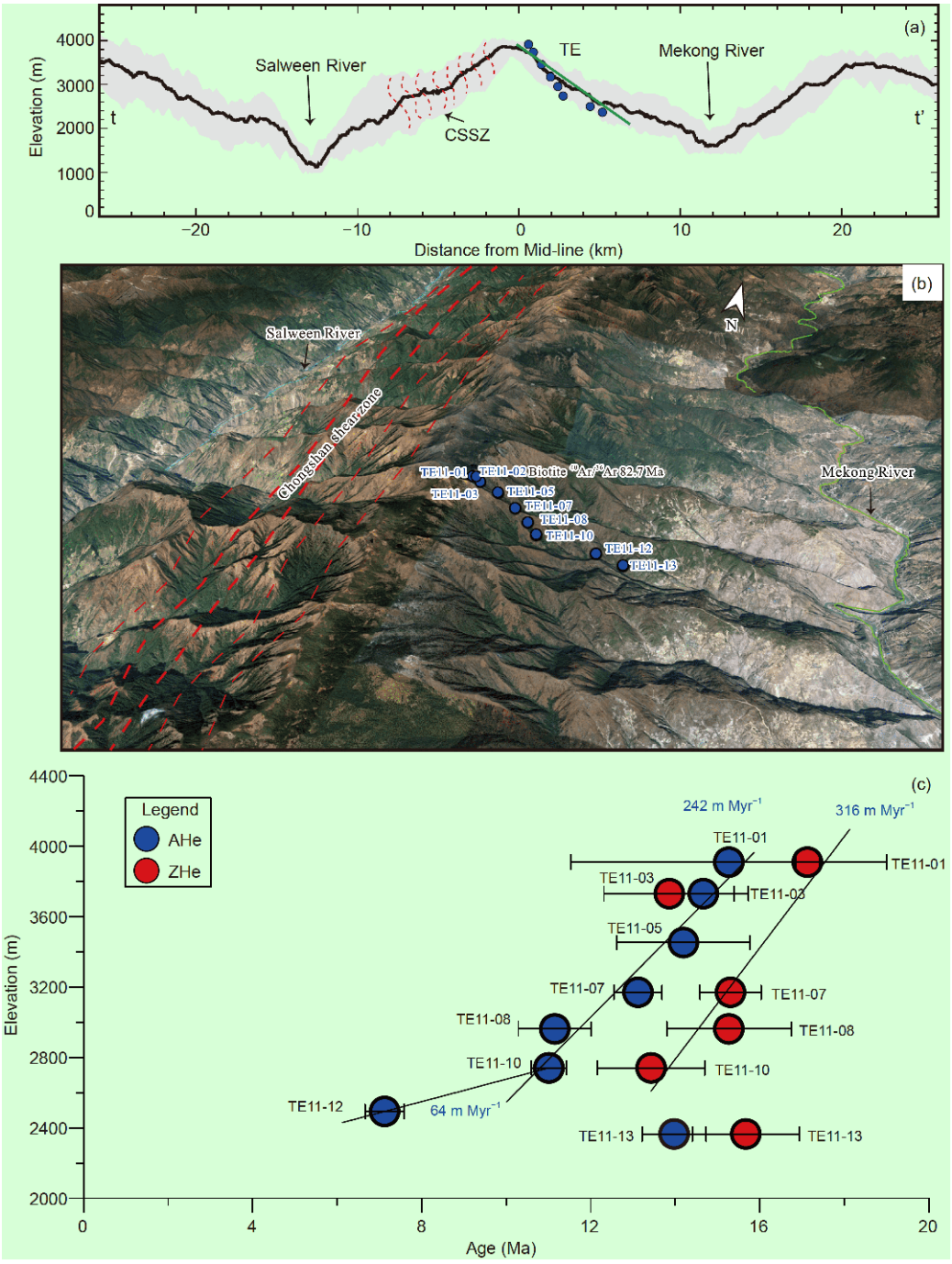

Figure 4 (a) Sample location on topographic swath profile. The swath profile t-t' shows the max, min and average topography, deep incision of major rivers, and the projected position of our samples. Circles are our new samples of TE profile. (b) The CSSZ location and sample locations are shown on the Google Earth image. (c) Plots of zircon and apatite (U-Th)/He ages against elevation and the exhumation rates according the age-elevation relationship for PM profile.

and Burchfiel, 1997; Ji et al., 2000; Xu et al., 2015) (Figures 1 and 2). This shear zone serves as form the western boundary of an extruded Indochina continental fragment (Ji et al., 2000; Wang et al., 2006; Akciz et al., 2008; Lin et al., 2009). The Gaoligong shear zone consists of two distinct units: an orthogneiss unit to the west and a metasedimentary unit to the east (Zhang et al., 2012a). The core of the Gaoligong shear zone consists of a narrow belt of mylonitic rocks with right-lateral strike-slip fabrics. Syn- to post-tectonic pegmatite dikes and tourmaline-bearing micaceous leucogranites are concentrated in the metasedimentary part of the Gaoligong shear zone. They have been affected by the same ductile deformation as their host mylonitic metamorphic rocks. However, the exact timing of the shearing remains

controversial (Akciz et al., 2008; Lin et al., 2009; Zhang et al., 2012b). The age of the activity and kinematics along the Gaoligong shear zone have been constrained by $^{40}Ar/^{39}Ar$ dating of synkinematic minerals and structural studies of ductile deformation. These studies indicate that the Gaoligong shear zone has been active since at least ~32 Ma (Ji et al., 2000; Wang et al., 2006; Lin et al., 2009; Zhang et al., 2012a). Strike-slip shearing continued until at least ~18 Ma, and perhaps to as late as ~14 Ma, and terminated at ~11 Ma (Ji et al., 2000; Akciz, 2004; Wang et al., 2006; Akciz et al., 2008; Lin et al., 2009; Zhang et al., 2012a). Huang et al. (2015) and Zhang et al. (2012a) identified four stages of deformation, which record the progressive transition from early ductile deformation associated with peak metamorphism, through ductile to ductile-brittle strike-slip shear deformation associated with exhumation.

The Chongshan shear zone is a 250-km long and 10-km wide metamorphic belt, which developed during early Cenozoic extrusion of the Indochina crustal fragment (Akciz et al., 2008; Zhang et al., 2010). The CSSZ consists mainly of mylonitic gneisses with amphibolite enclaves, leucogranites, migmatites, pegmatites, marbles and garnet-bearing schists with well-defined foliation parallel to the trend of the zone (Zhang et al., 2009, 2010, 2011). Based on available zircon U-Pb, monazite U-Th/Pb, and muscovite $^{40}Ar/^{39}Ar$ ages, Zhang et al. (2012b) reported that transpressional deformation was initiated during the interval of 57–46 Ma, and that strike-slip shearing may have begun at 34–32 Ma (Wang et al., 2006; Akciz et al., 2008; Zhang et al., 2010, 2012b). Geochronological studies by Akciz et al. (2008) indicated that the Chongshan shear zone terminated by ~17 Ma. Petrological and thermobarometric studies of the Chongshan shear zone reveal two metamorphic stages during the interval of ~36–14 Ma: an early upper-amphibolite facies event and a later greenschist facies overprint (Wang et al., 2006; Akciz et al., 2008; Zhang et al., 2012a). Zhang et al. (2010) proposed that the contrasting shear sense of the two segments was caused by regional-scale strain partitioning of sinistral transpression (Zhang et al., 2010; Huang et al., 2015).

Previous studies about the exhumation of shear zones are increasingly recognized as providing important information about their evolution (see references in Oriolo et al., 2018). Existing low-temperature thermochronometric data have elucidated the detailed pattern of erosion in the Three Rivers Region. The data from upland areas indicate Cretaceous cooling (Wilson and Fowler, 2011; Tian et al., 2014; Liu-Zeng et al., 2018). Significant Cenozoic exhumation came from river valley or major strike-slip faults from the Miocene to the Holocene (Ouimet et al., 2010; Shen et al., 2016; Yang et al., 2016; Nie et al., 2018; Wang et al., 2018). Sparse data suggest that some locations may have experienced the effect of structurally enhanced rock denudation and shearing or fault-related hydrothermal reheating (Wang et al., 2016, 2018).

3. Sampling and methods

3.1 Sample selection

In order to constrain the crystallization age and subsequent exhumation history of the granitoid rocks in the Langcang-Mekong River and Nu Jiang-Salween River region and their relationship with the shear zones, we used zircon U/Pb, biotite $^{40}Ar/^{39}Ar$, and ZHe and AHe dating.

Eighteen granitic or granite gneiss samples were collected from two near vertical profiles (the PM profile and the TE profile) on the western banks of the Nu Jiang-Salween River near Pianma and the Langcang-Mekong River near Tu'er (Figures 1 and 2). The PM profile yielded nine samples between 1600 and 3500 m. The PM profile crosses the Gaoligong shear zone and consists of a lower part (the PM_i profile), with five samples within the Gaoligong shear zone, and an upper part (the PM_o profile), with four samples to the west of the shear zone. The highest sample (PM11-03) was collected from a ridge with the elevation of 3490 m. The lowermost sample is from 1673 m, 850 m above the Nu Jiang-Salween River. The TE profile, located to the east of the Chongshan shear zone, comprises 9 samples from between 2300 and 3900 m. The average vertical separation between samples is 150–300 m, and the lowermost sample is 900 m above the Langcang-Mekong River. Detailed information about the samples is given in Table 1.

3.2 Zircon U-Pb and biotite $^{40}Ar/^{39}Ar$ geochronology

We sampled granitic rocks in the PM and TE profiles for U-Pb dating, in order to verify whether a late magmatic event could have affected the geothermal field. Two samples (PM11-05 and PM11-26) from the PM profile, and sample TE11-02 from the TE profile, were collected for zircon U-Pb dating. The three samples yielded data interpreted to be the crystallization ages of the rocks. Zircon U-Pb dating was performed by laser-ablation ICP-Q-MS at the Key Laboratory of Metallogeny and Mineral Assessment, Institute of Mineral RESOURCES, CAGS. Laser sampling was conducted using a GeoLas 2005 System with a spot size of 32 μm. An Agilent 7500a ICP-MS instrument was used to acquire ion-signal intensities. Instrumental conditions and data acquisition are comprehensively described by Wu et al. (2006) and Hou et al. (2009).

Higher temperature (>300°C) thermochronological information was obtained from biotite Ar isotopic data. We determined two $^{40}Ar/^{39}Ar$ ages of biotite from granitic rocks from the tops of the PM profile and the TE profile. $^{40}Ar/^{39}Ar$ dating of biotite was performed at the Institute of Tibetan Plateau Research, Chinese Academy of Sciences. Biotite

Table 1 Geological information of samples from PM and TE profiles and a summary of U-Pb, $^{40}Ar/^{39}Ar$, AHe and ZHe ages[a)]

Sample ID*	Longitude	Latitude	Elevation (m)	Lithology	U-Pb±1σ (Ma)	$^{40}Ar/^{39}Ar$±1σ (Ma)	Mean AHe±1σ (Ma)	Mean ZHe±2σ (Ma)
Pianma (PM)								
PM11-01	98.74936°N	25.95028°E	2241	Granodiorite			9.9±1.3	12.8±1.3
PM11-03	98.69059°N	25.99679°E	3490	Granite			14.1±1.4	20.7±3.1
PM11-05	98.69405°N	25.9921°E	3260	Granite	120.7±2.7	47.47±0.68	13.4±0.6	19.2±2.7
PM11-07	98.69727°N	25.98777°E	3060	Granite			12.6±0.4	16.2±1.5
PM11-21	98.74694°N	25.95722°E	2677	Granite gneiss				12.1±0.9
PM11-23	98.74697°N	25.95203°E	2399	Granite gneiss			9.5±4.5*	
PM09-25	98.74772°N	25.94639°E	1951	Granite gneiss			6.0±0.9	
PM11-26	98.74689°N	25.9443°E	1777	Granodiorite	117±1.1			
PM11-28	98.75628°N	25.93947°E	1673	Granite gneiss				11.9±1.5
Tu'er (TE)								
TE11-01	99.02539°N	26.37009°E	3909	Monzonitic granite			15.3±3.7	87.2±96.7*
TE11-02	99.02685°N	26.3694°E	3810	Granite	209.8±6.1	82.75±1.28		
TE11-03	99.0279°N	26.3693°E	3730	Granite			14.7±1.1	13.8±1.5
TE11-05	99.03315°N	26.36925°E	3452	Granite			14.2±1.6	
TE11-07	99.03855°N	26.36748°E	3170	Granite			13.1±0.6	15.3±0.7
TE11-08	99.0428°N	26.36499°E	2962	Granite			11.2±0.9	15.3±1.5
TE11-10	99.0459°N	26.36228°E	2740	Granite			11.0±0.4	13.4±1.3
TE11-12	99.06253°N	26.36103°E	2493	Granite			7.1±0.5	
TE11-13	99.07003°N	26.36028°E	2365	Granite			14.0±0.8	15.7±1.3

a) For PM11-01 and TE11-01 samples, AHe are multi-grain measurements, with two replicates. For other samples, the measurements were conducted for both apatite and zircon, with three replicates. Listed are the weighted mean ages, which were calculated using Isoplot/Ex_ver3 (Ludwig, 2003). The weighted mean ages with "*" were calculated with their scattered ages.

separates were obtained using conventional methods and were purified by hand-picking under a binocular microscope. Samples were heated stepwise from 750 to 1450°C to produce well-defined plateau ages. The procedures followed for these isotope analyses were the same as those described by Sang et al. (1996).

3.3 (U-Th)/He analysis

Eight samples from the PM profile and 8 samples from the TE profile, spanning the elevation range of 2500–5000 m, were analyzed for ZHe and AHe ages (Tables 2 and 3). All of the (U-Th)/He analyses were conducted at the University of Arizona. All granitic samples targeted for ZHe or AHe were crushed and sieved following standard procedures, and zircon and apatite grains within the 100–300 μm fraction were isolated using heavy liquids. For AHe and ZHe dating, euhedral crystals were selected under a high-power polarized light stereo-zoom binocular microscope to detect the possible presence of small inclusions. For each sample, at least three euhedral apatite crystals containing minimal inclusions were selected for single crystal (U-Th)/He measurements. First, a camera was used to take high-resolution digital photographs for alpha-ejection corrections (Farley et al., 1996). The apatite and zircon crystals were then loaded in Pt (apatite) and Nb (zircon) microtubes and outgassed under ultra-high vacuum using a diode laser by heating at 960 and 1250°C, respectively. Degassed aliquots were dissolved and U and Th concentrations were measured by isotope dilution using a sector inductively coupled plasma mass spectrometer.

3.4 Calculation of exhumation rates

Four methods were used to calculate the cooling and exhumation rates: the age-elevation relationship (AER) method (Fitzgerald et al., 1999; Braun, 2002; Gallagher et al., 2005); the analytical method proposed by Willett and Brandon's (2013); QTQt modeling (Gallagher, 2012); and the three-dimensional finite-element thermal-kinematic method (Pecube) (Braun et al., 2012). Each method has its strength and limitations, but by combining them, we hoped to determine the exhumation history of our samples.

Age-elevation data are commonly used to determine exhumation rates assuming temporally and spatially invariant horizontal isotherms (Wagner and Reimer, 1972). In this case, the slope of the regression line in age-elevation plots can be interpreted as the exhumation rate. A one-dimensional

Table 2 Results of single-grain zircon (U-Th)/He dating of samples from PM and TE profile[a)]

Sample number	U (ppm)	Th (ppm)	Th/U	eU (ppm)	^{4}He (nmol g^{-1})	Rs (μm)	Raw age (Ma)	1σ (Ma)	Ft	Corrected age (Ma)	1σ (Ma)	Weighted mean age±2σ (Ma)
Pianma (PM)												
PM11-01_Zr1	472.08	261.82	0.57	533.61	26.47	64.72	9.2	0.6	0.81	11.4	0.2	
PM11-01_Zr2	455.23	143.56	0.32	488.97	29.80	67.54	11.3	0.7	0.82	13.9	0.2	12.8±1.3
PM11-01_Zr3	600.99	354.82	0.61	684.38	40.61	73.18	11.0	0.7	0.83	13.3	0.2	
PM11-03_Zr1	460.47	224.50	0.50	513.23	38.58	61.43	13.9	0.8	0.80	17.5	0.3	
PM11-03_Zr2	445.85	182.72	0.42	488.79	45.06	69.57	17.1	1.0	0.82	20.8	0.3	20.7±3.1
PM11-03_Zr3	511.47	302.69	0.61	582.60	57.27	53.29	18.2	1.1	0.77	23.7	0.4	
PM11-05_Zr1	608.10	136.47	0.23	640.17	56.69	63.77	16.4	1.0	0.81	20.4	0.3	
PM11-05_Zr2	870.24	279.66	0.33	935.96	63.83	57.03	12.6	0.8	0.78	16.1	0.2	19.2±2.7
PM11-05_Zr3	1638.27	631.10	0.40	1786.58	160.81	58.29	16.7	1.0	0.79	21.2	0.3	
PM11-07_Zr1	870.72	331.80	0.39	948.70	73.52	81.21	14.4	0.9	0.84	17.0	0.3	
PM11-07_Zr2	823.08	433.57	0.54	924.97	72.97	88.84	14.6	0.9	0.86	17.1	0.3	16.2±1.5
PM11-07_Zr3	802.87	174.45	0.22	843.87	56.23	88.13	12.4	0.7	0.86	14.4	0.2	
PM11-21_Zr1	1015.28	347.67	0.35	1096.98	59.01	65.19	10.0	0.6	0.81	12.3	0.2	
PM11-21_Zr2	992.48	554.40	0.57	1122.77	60.27	55.32	9.9	0.6	0.78	12.8	0.2	12.1±0.9
PM11-21_Zr3	1130.05	410.29	0.37	1226.47	55.41	48.29	8.4	0.5	0.75	11.2	0.2	
PM11-28_Zr1	442.42	190.61	0.44	487.21	26.11	54.19	9.9	0.6	0.77	12.9	0.2	
PM11-28_Zr2	298.95	153.55	0.53	335.03	14.22	55.49	7.9	0.5	0.78	10.1	0.1	11.9±1.5
PM11-28_Zr3	1169.71	251.75	0.22	1228.88	61.72	45.27	9.3	0.6	0.73	12.7	0.2	
Tu'er (TE)												
TE11-01_Zr1	349.90	119.85	0.35	378.07	68.99	43.05	33.8	2.0	0.72	46.9	0.7	
TE11-01_Zr2	1256.95	127.48	0.10	1286.91	81.72	37.98	11.8	0.7	0.69	17.1	0.3	17.1±0.3
TE11-01_Zr3	1079.45	320.25	0.30	1154.71	864.39	38.71	137.2	8.2	0.69	197.5	2.8	
TE11-03_Zr1	452.32	98.32	0.22	475.42	28.66	69.10	11.2	0.7	0.82	13.6	0.2	
TE11-03_Zr2	453.21	43.52	0.10	463.44	26.49	84.15	10.6	0.6	0.85	12.5	0.2	13.8±1.5
TE11-03_Zr3	618.17	97.73	0.16	641.13	43.18	64.29	12.5	0.7	0.81	15.5	0.2	
TE11-07_Zr1	716.19	127.75	0.18	746.21	54.06	114.90	13.4	0.8	0.89	15.1	0.2	
TE11-07_Zr2	1151.77	145.07	0.13	1185.87	88.12	88.46	13.8	0.8	0.86	16.1	0.2	15.3±0.7
TE11-07_Zr3	676.91	134.38	0.20	708.49	48.15	85.97	12.6	0.8	0.85	14.8	0.2	
TE11-08_Zr1	518.10	128.42	0.25	548.28	38.72	64.17	13.1	0.8	0.81	16.2	0.2	
TE11-08_Zr2	1021.67	107.71	0.11	1046.98	70.41	55.74	12.5	0.7	0.78	16.0	0.2	15.3±1.5
TE11-08_Zr3	337.58	109.35	0.33	363.28	20.37	51.99	10.4	0.6	0.76	13.6	0.2	
TE11-10_Zr1	585.54	182.29	0.32	628.38	39.42	59.58	11.6	0.7	0.79	14.7	0.2	
TE11-10_Zr2	774.13	264.22	0.35	836.22	42.74	55.52	9.5	0.6	0.78	12.2	0.2	13.4±1.3
TE11-10_Zr3	283.50	56.81	0.21	296.85	17.38	64.87	10.9	0.7	0.81	13.4	0.2	
TE11-13_Zr1	258.18	61.67	0.25	272.68	19.59	59.06	13.3	0.8	0.79	16.8	0.3	
TE11-13_Zr2	572.64	32.25	0.06	580.22	35.83	60.42	11.5	0.7	0.80	14.4	0.2	15.7±1.3
TE11-13_Zr3	701.13	134.67	0.20	732.77	52.17	76.07	13.2	0.8	0.84	15.8	0.2	

a) All samples run three replicates. The weighted mean calculations were made using soplot/Ex_ver3 (Ludwig, 2003), weighted by age uncertainties of individual grains.

steady-state model presented by Willett and Brandon (2013) is based on the assumption of a constant rate of exhumation, where the observed ages represent the time taken for a sample to travel from its closure depth to its modern elevation. Importantly, this method relaxes the assumption inherent in the AER approach and allows for transient geothermal gradients that evolve due to changing exhumation rates. The 1D method transforms each age into a relationship in the geothermal gradient and exhumation rate space illustrated by graphical curves.

We modeled time-temperature histories of the PM and TE profiles using QTQt software (v5.4.0; Gallagher, 2012), based on the Bayesian transdimensional Markov chain Monte Carlo inversion approach. Unlike the two approaches

Table 3 Results of single-grain apatite (U-Th)/He dating of samples from PM and TE profiles[a)]

Sample name	U (ppm)	Th (ppm)	Th/U	Sm (ppm)	eU (ppm)	^{4}He (nmol g^{-1})	Rs (μm)	Raw age (Ma)	1σ (Ma)	Ft	Corr. age (Ma)	1σ (Ma)	Weighted mean age±2σ (Ma)
Pianma (PM)													
PM11-01_Ap1	17.25	26.10	1.55	134.31	23.39	0.81	45.79	6.5	0.7	0.68	9.5	1.0	9.9±1.3
PM11-01_Ap3	23.65	49.02	2.13	257.70	35.17	1.44	58.19	7.6	0.7	0.74	10.3	0.5	
PM11-03_Ap1	23.46	66.03	2.89	312.94	38.98	2.10	43.11	10.0	0.6	0.66	15.1	0.3	
PM11-03_Ap2	33.60	47.36	1.45	306.23	44.73	1.80	34.00	7.5	0.5	0.59	12.8	0.9	14.1±1.4
PM11-03_Ap3	28.48	32.49	1.17	730.60	36.11	1.73	36.18	8.8	0.5	0.61	14.4	0.3	
PM11-05_Ap1	14.94	41.72	2.87	307.66	24.74	1.24	45.06	9.2	0.6	0.67	13.7	0.5	
PM11-05_Ap2	10.85	28.74	2.72	285.60	17.6	0.80	41.44	8.3	0.5	0.65	12.9	0.3	13.4±0.6
PM11-05_Ap3	24.04	51.88	2.21	339.53	36.23	1.62	37.05	8.3	0.5	0.61	13.5	0.2	
PM11-07_Ap1	14.32	37.99	2.72	300.96	23.24	1.16	55.12	9.2	0.6	0.73	12.7	0.2	
PM11-07_Ap2	24.82	60.77	2.51	431.29	39.11	1.82	44.32	8.6	0.5	0.67	12.9	0.2	12.6±0.4
PM11-07_Ap3	16.42	42.73	2.67	333.18	26.46	1.28	54.91	8.9	0.5	0.73	12.3	0.2	
PM11-23_Ap1	6.75	8.55	1.30	19.69	8.76	0.50	58.47	10.6	0.6	0.75	14.3	0.3	
PM11-23_Ap2	5.57	5.86	1.08	24.04	6.94	0.15	57.02	4.0	0.2	0.74	5.4	0.2	9.5±4.5
PM11-23_Ap3	7.02	6.57	0.96	29.53	8.57	0.30	59.97	6.6	0.4	0.75	8.7	0.2	
PM11-25_Ap1	5.83	15.45	2.72	47.28	9.46	0.26	60.78	5.1	0.3	0.75	6.8	0.2	
PM11-25_Ap2	6.62	15.65	2.43	23.71	10.3	0.22	45.12	3.9	0.2	0.67	5.8	0.5	6±0.9
PM11-25_Ap3	6.79	21.03	3.18	46.38	11.73	0.23	48.30	3.7	0.2	0.69	5.3	0.5	
Tu'er (TE)													
TE11-01_Ap2	1.79	2.24	1.28	38.97	2.32	0.13	35.77	10.4	0.6	0.61	17.1	2.2	15.3±3.7
TE11-01_Ap3	1.38	0.71	0.53	40.91	1.54	0.08	44.56	9.2	0.5	0.68	13.4	1.5	
TE11-03_Ap1	137.27	6.78	0.05	251.64	138.86	8.71	58.42	11.9	0.7	0.75	15.8	0.2	
TE11-03_Ap2	175.70	14.47	0.08	284.36	179.1	9.79	49.39	10.3	0.6	0.71	14.5	0.2	14.7±1.1
TE11-03_Ap3	149.57	9.09	0.06	257.41	151.7	7.94	51.45	9.9	0.6	0.72	13.7	0.2	
TE11-05_Ap1	236.17	18.73	0.08	302.94	240.57	12.98	72.68	10.2	0.6	0.80	12.8	0.2	
TE11-05_Ap2	112.14	6.50	0.06	294.66	113.67	7.47	67.15	12.4	0.7	0.78	15.9	0.2	14.2±1.6
TE11-05_Ap3	94.83	4.86	0.05	203.21	95.97	5.57	68.52	11.0	0.7	0.79	13.9	0.2	
TE11-07_Ap1	71.69	5.66	0.08	221.08	73.03	4.42	110.06	11.4	0.7	0.87	13.2	0.4	
TE11-07_Ap2	114.18	20.80	0.19	235.73	119.07	6.42	62.34	10.2	0.6	0.77	13.3	0.5	13.1±0.6
TE11-07_Ap3	162.34	22.02	0.14	281.28	167.51	9.15	75.49	10.3	0.6	0.81	12.8	0.4	
TE11-08_Ap1	62.53	7.16	0.12	204.96	64.22	2.82	54.00	8.3	0.5	0.74	11.3	0.5	
TE11-08_Ap2	59.82	6.43	0.11	221.28	61.33	2.62	46.49	8.1	0.5	0.70	11.6	0.6	11.2±0.9
TE11-08_Ap3	32.37	3.33	0.11	122.42	33.15	1.38	55.72	7.8	0.5	0.74	10.5	0.6	
TE11-10_Ap1	128.56	4.79	0.04	177.52	129.68	5.98	81.95	8.7	0.5	0.82	10.6	0.2	
TE11-10_Ap2	171.81	19.55	0.12	213.73	176.4	8.58	79.99	9.2	0.6	0.82	11.3	0.2	11±0.4
TE11-10_Ap3	153.40	1.61	0.01	211.16	153.78	6.75	57.17	8.3	0.5	0.75	11.1	0.2	
TE11-12_Ap1	33.37	62.45	1.92	416.58	48.05	1.36	50.54	5.3	0.3	0.71	7.4	0.1	
TE11-12_Ap2	11.90	17.27	1.49	190.41	15.96	0.40	46.05	4.7	0.3	0.69	6.8	0.1	7.1±0.5
TE11-12_Ap3	28.86	159.64	5.68	166.67	66.37	14.36	59.35	40.1	2.4	0.74	54.3	0.6	
TE11-13_Ap1	130.70	14.41	0.11	288.86	134.08	7.36	56.37	10.4	0.6	0.75	13.9	0.6	
TE11-13_Ap2	150.46	18.12	0.12	333.77	154.71	8.29	58.90	10.1	0.6	0.76	13.4	0.3	14±0.8
TE11-13_Ap3	121.48	4.67	0.04	199.71	122.58	7.28	63.82	11.3	0.7	0.77	14.5	0.3	

a) The mean age was calculated using Isoplot/Ex_ver3 (Ludwig, 2003), weighted by age uncertainties of individual grains.

described above, this approach allows us to identify complex cooling histories; however, a thermal model is needed to convert the cooling histories to the exhumation rate history. The ZHe and AHe data from each transect are modeled jointly. ZHe and AHe data were jointly inverted taking into account radiation damage accumulation and the annealing models of Guenthner et al. (2013) and Flowers et al. (2009), respectively. The initial temperature constraint was set to 310 ±50°C at 18 Ma for the PM_i profile, 47.4 Ma for the PM_o profile, and 82.7 Ma for the TE profile, according to the

corresponding biotite $^{40}Ar/^{39}Ar$ data for granitoids. All model results represent 200000 iterations: 100000 iterations were used during the burn-in phase of the inversion process, and the second 100000 iterations were used to approximate the posterior probability density functions (Gallagher, 2012).

We used the three-dimensional finite-element thermal-kinematic code (Pecube) to quantify the exhumation history. The TE, PM_i and PM_o profiles were treated as independent profiles. Pecube solves the heat equation and tracks material points that reach the surface of the model through the evolving thermal conditions. This produces time-temperature paths that are used to calculate apparent thermochronometric ages. In our model, we used the value of 50 km for the lower boundary, which is similar to the present thickness of the crust in the southeastern Tibetan Plateau, and corresponds to the crustal thickness in the study area. We used a basal temperature of 500–1000°C, a radiogenic heat production rate of 10°C Myr^{-1}, thermal diffusivity of 25 km^2 Myr^{-1}, and an atmospheric lapse rate of 4°C km^{-1} (Bermúdez et al., 2011). In order to better constrain the recent exhumation history, the Pecube program was run for two crustal blocks of roughly 10 km×10 km around the PM_i, PM_o, and TE profiles. Details of the parameters used in the models are listed in Appendix Table S1 (https://link.springer.com).

4. Analytical results

4.1 Zircon U-Pb and biotite $^{40}Ar/^{39}Ar$ geochronology

Three samples (PM11-05, PM11-26 and TE11-02) were dated using zircon U-Pb ICP -MS. Zircon U-Pb dating of sample PM11-26 yielded a concordant intercept age of 117 ±1.1 Ma (MSWD=1.5; Figure 5), which is interpreted as the crystallization age, while sample PM11-05 yielded a low-quality concordant intercept age of 120.7±2.7 Ma. The zircon U-Pb age of sample TE11-02 is 209.8±6.1 Ma. We analyzed two samples for biotite $^{40}Ar/^{39}Ar$ ages: PM11-05 from the PM profile and TE11-02 from the TE profile. The biotite $^{40}Ar/^{39}Ar$ ages of samples PM11-05 and TE11-02 are 47.47±0.68 and 82.75±1.28 Ma, respectively (Figure 6). The microstructures of samples PM11-05 and TE11-02 indicate that they did not experience noticeable deformation (Figure 6). The detailed U-Pb and $^{40}Ar/^{39}Ar$ dating results are listed in Appendix Table S2.

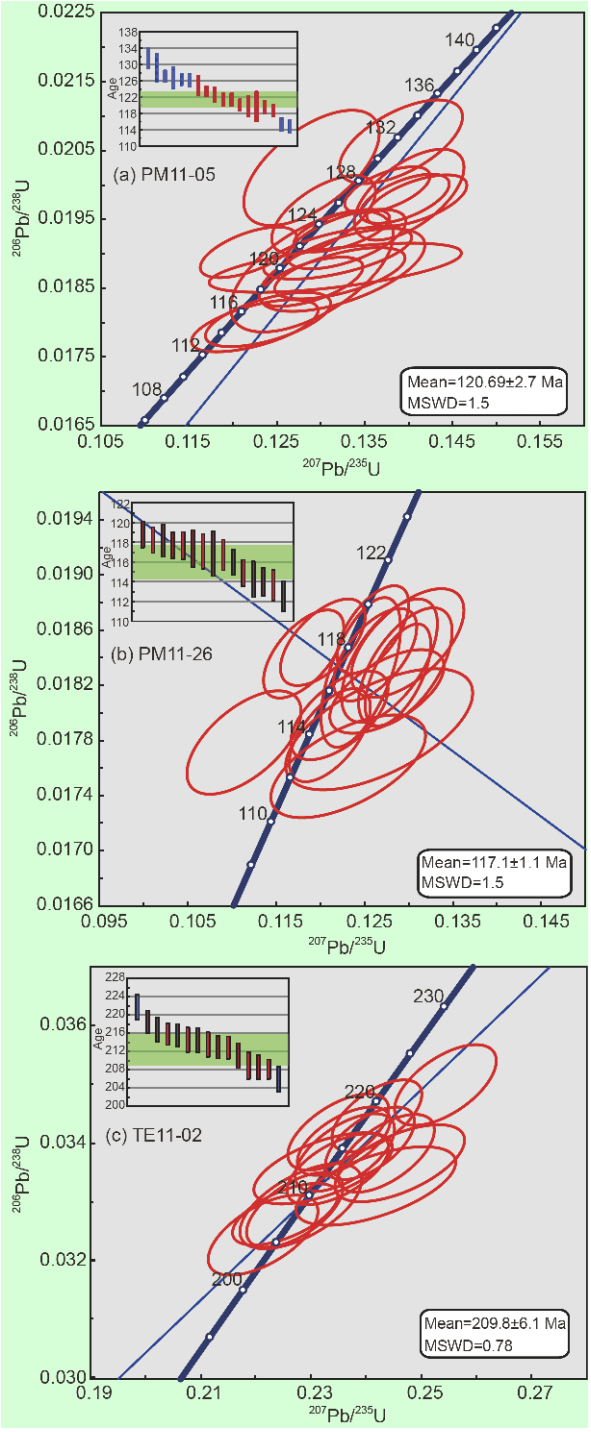

Figure 5 Zircon U-Pb concordia and weighted mean ages diagrams for the samples PM11-05, PM11-26, and TE11-02. Inserts are weighted mean diagrams. MSWD is the mean standard weighted deviation.

4.2 (U-Th)/He thermochronological results

The weighted mean zircon and apatite (U-Th)/He ages were calculated from 2–3 single grain ages per sample (Tables 2 and 3). Five apatite samples yielded AHe ages of 6.0–14.1 Ma from the PM profile, except for sample PM11-23, which yielded three scattered ages (with the range of 5.4–14.3 Ma). One two-grain apatite AHe age of the sample PM11-01 is 9.9 Ma and six three-grain zircon samples yielded ZHe ages with the range of 11.9–20.7 Ma.

The TE profile consists of nine samples spanning the elevation range of 2300–3900 m (Table 1). The mean AHe ages of seven three-grain samples and one two-grain sample range from 7.1–15.3 Ma. The mean ZHe ages for six three-

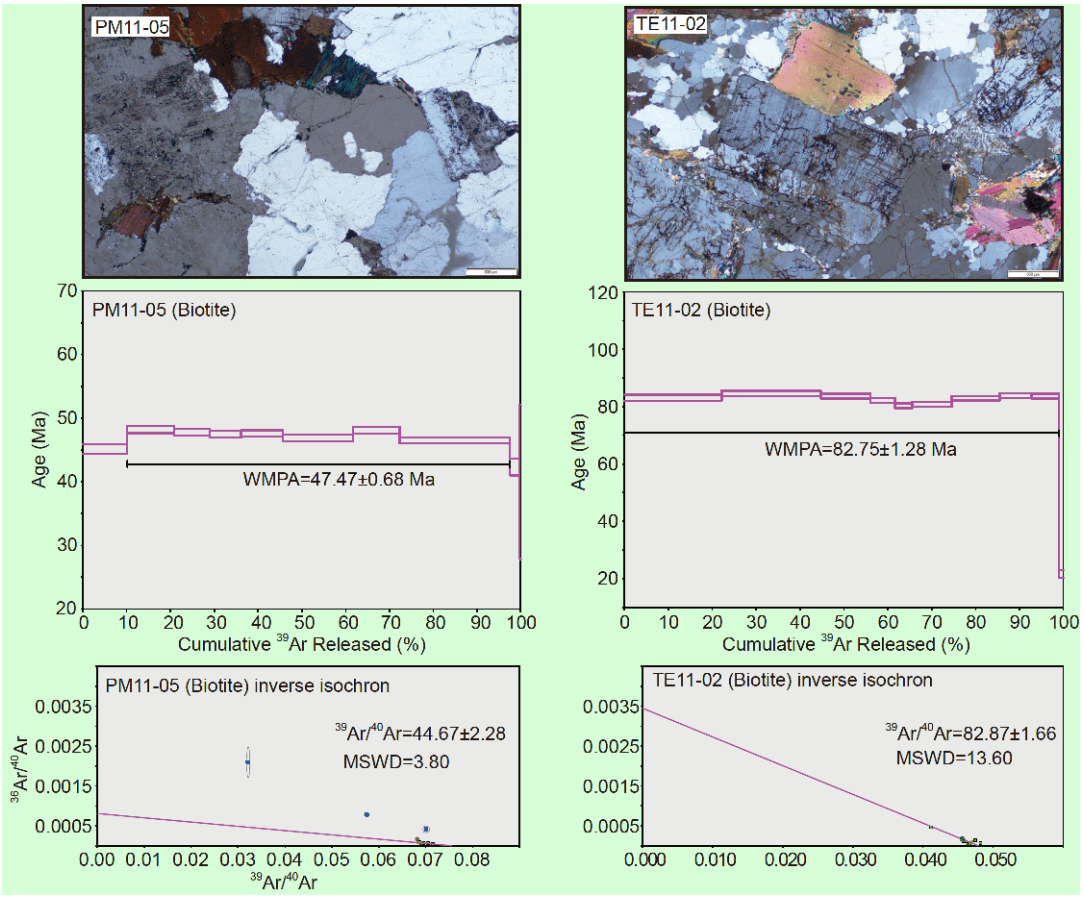

Figure 6 Photomicrographs, apparent ages spectra, and inverse isochron age from samples TE11-02 and PM11-05. WMPA-weighted mean plateau age. MSWD-mean standard weighted deviation.

grain samples are within the range of 13.8–15.7 Ma, except for one outlier (TE11-01) with three scattered ages (with the range of 17.1–197.5 Ma). For both profiles, the single-grain AHe and ZHe ages versus eU (effective uranium content) plots do not show clear relationships (Figure 7).

For the PM and TE profiles, most of the AHe and ZHe ages increase as the elevation increased. In general, the AHe and ZHe ages of the TE profile yield a better age-elevation correlation than the PM profile. However, the ZHe ages of sample PM11-21 (from the PM profile) and sample TE11-03 (from the TE profile) lack a clear age-elevation correlation (Figure 4). We interpret the ZHe ranges of samples PM11-21 and TE11-03 to reflect much greater effects on He diffusivity and thermal sensitivity of the zircon (U-Th)/He system than crystallographic anisotropy because of radiation damage (Guenthner et al., 2013).

5. Interpretation of the exhumation rate and exhumation history

In order to improve the interpretation of the cooling ages described above, we calculated the exhumation and cooling rates for the PM_i, PM_o and TE profiles based on the four methods described in Section 3.4.

5.1 Lower part of the PM profile (PM_i)

Our new data exhibit positive correlations between age and elevation, with the exception of the ZHe age of sample PM11-21 from the PM profile. In the PM_i profile, the age-elevation relationship of our ZHe data suggests an exhumation rate of 0.09 km Myr^{-1} during the interval of 20.7–16.2 Ma, and that of the AHe ages yields an exhumation rate of 0.28 km Myr^{-1} during the interval of 14.1–12.6 Ma (Figure 3).

The QTQt model of PM_i suggests two periods of cooling. A major cooling phase began during the interval of 18–6 Ma, with a cooling rate of >20°C Myr^{-1} or >0.5 km Myr^{-1} (Figure 8), followed by a slow cooling rate (<10°C Myr^{-1}); however, this is not consistent with the exhumation rate based on the age-elevation relationship.

We used four samples and six published data from Wang et al. (2018) to run the 3D inversion model and to run Pecube to assess the exhumation rates of the PM_i profile. All samples are located in the shear zone in the PM_i profile. We used two

published biotite $^{40}Ar/^{39}Ar$ ages of 17.6 and 17.9 Ma (Lin et al., 2009) to constrain the high temperature cooling. Because the thermochronometric ages in our dataset are all younger than 18 Ma, the starting time of the model was set as 18 Ma. Initially, the exhumation rate history was calculated with uniform time steps of 2 Myr. This initial inversion was used to identify the number of possible time transition nodes so that a second Pecube inversion could be carried out. The aim of this second inversion was to determine the precise timing of changes in exhumation rate. We assumed a three-stage cooling history with two transition times based on the results of the age-elevation relationship and the exhumation rate of the model for the 2-Myr-interval.

The Pecube inversion results show that a three-stage history fits the data quite well. The exhumation rate of the first stage (E_1) is between 1.2 and 1.7 km Myr^{-1} (Figure 9). The best-fit solutions have an onset time (T_2) of the second exhumation stage with the range of 10–11 Ma, with a maximum probability at 10.2 Ma (Figure 9). The onset time of the third exhumation stage (T_3) has the ranges of 0–4 Ma and the optimal solution of T_3 between 3 and 4 Ma. The exhumation rate of E_3 is between 0.0 and 0.4 km Myr^{-1}, which is slightly higher than that of E_2 (0.0–0.2 km Myr^{-1}). Detailed information about Pecube is given in Appendix Table S1.

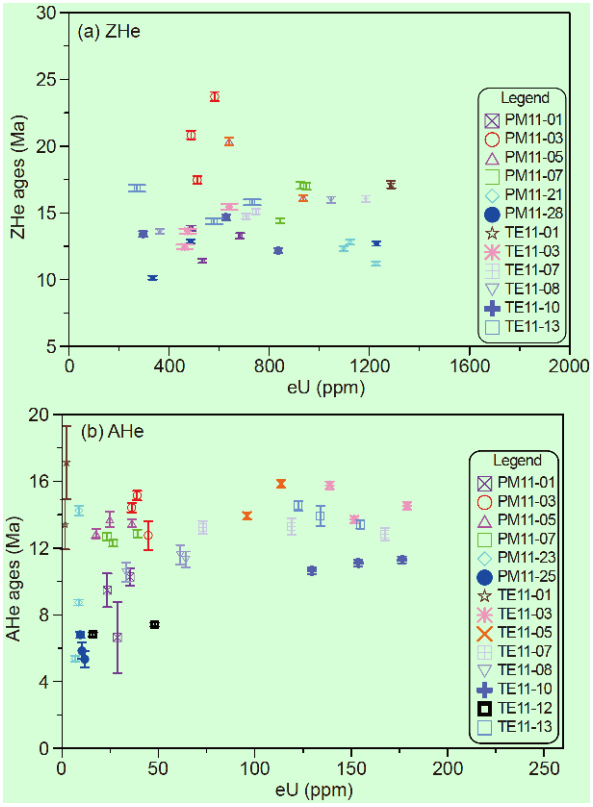

Figure 7 Corrected ZHe or AHe ages versus effective uranium content [eU].

5.2 Upper part of the PM profile (PM_o)

In profile PM_o, the exhumation rate was 0.47 km Myr^{-1} during the interval of 12.8–11.9 Ma, as indicated by the ZHe age-elevation relationship method, and 0.09 km Myr^{-1} during the interval of 9.9–6 Ma estimated from the AHe ages and their elevation (Figure 3). The QTQt model for profile PM_o suggests a three-stage thermal history (Figure 8): a first stage of cooling during the interval of 47.4–16 Ma with a cooling rate of <5°C Myr^{-1}; a second cooling stage during the interval of 19–12.5 Ma at a cooling rate of >30°C Myr^{-1}; and a third stage after 12.5 Ma, during which the cooling rate decreased substantially to <0.5°C Myr^{-1}.

The Pecube model for the PM_o profile is constrained by ZHe and AHe ages from four samples (one sample, NJ008, is from Wang et al. (2018)). Modeling of a three-phase scenario was conducted with a search for the best solutions of the timing of onset and the exhumation rate, guided by the exhumation rate of the model for the 3-Myr-interval (Table S1) and the age-elevation profile of the thermochronological data. The onset time of this model is 21 Ma according to the oldest ZHe age. The best-fit solutions have T_2 with the range of 8–21 Ma with a maximum probability at 16 Ma (Figure 9). The corresponding exhumation rate E_1 has the range of 0.39–0.63 km Myr^{-1}. The exhumation rate E_2 decreased to between 0.05 and 0.19 km Myr^{-1} since ~16 Ma. The timing of the end of the second stage (T_3) is between 4.8 and 6.3 Ma and the exhumation increased after 4.8–6.3 Ma. The exhumation rate of the third stage has the range of 0.38–0.6 km Myr^{-1}.

In this model, there are two important exhumation transition nodes: at 15–17 and 5–6 Ma. The exhumation rate of the second stage is lower than that of the other stages. In order to provide an independent estimate of the exhumation rate, we used the analytical method of Willett and Brandon (2013), as described in Section 3.4. The ages of the lowest and oldest sample are used as the start and end times of each time interval, respectively, as illustrated by Willett and Brandon (2013). For the ZHe data, an exhumation rate of 0.32–0.72 km Myr^{-1} is predicted for the time interval between 21 and 16 Ma in the PM_o profile. For the AHe data, the predicted exhumation rate is 0.15–0.25 km Myr^{-1} during the interval of ~14–12 Ma in the PM_o profile (Figure 10).

5.3 TE profile

The new data for the TE profile show positive correlations between age and elevation, with the exception of two ages (the ZHe age of sample TE11-03 and the AHe and ZHe ages of sample TE11-13). The exhumation rate was 0.24–0.32 km Myr^{-1} during the interval of 18–11 Ma, followed by a decrease to 0.06 km Myr^{-1} during the interval of 11–6 Ma, based on AHe and ZHe age-elevation relationship.

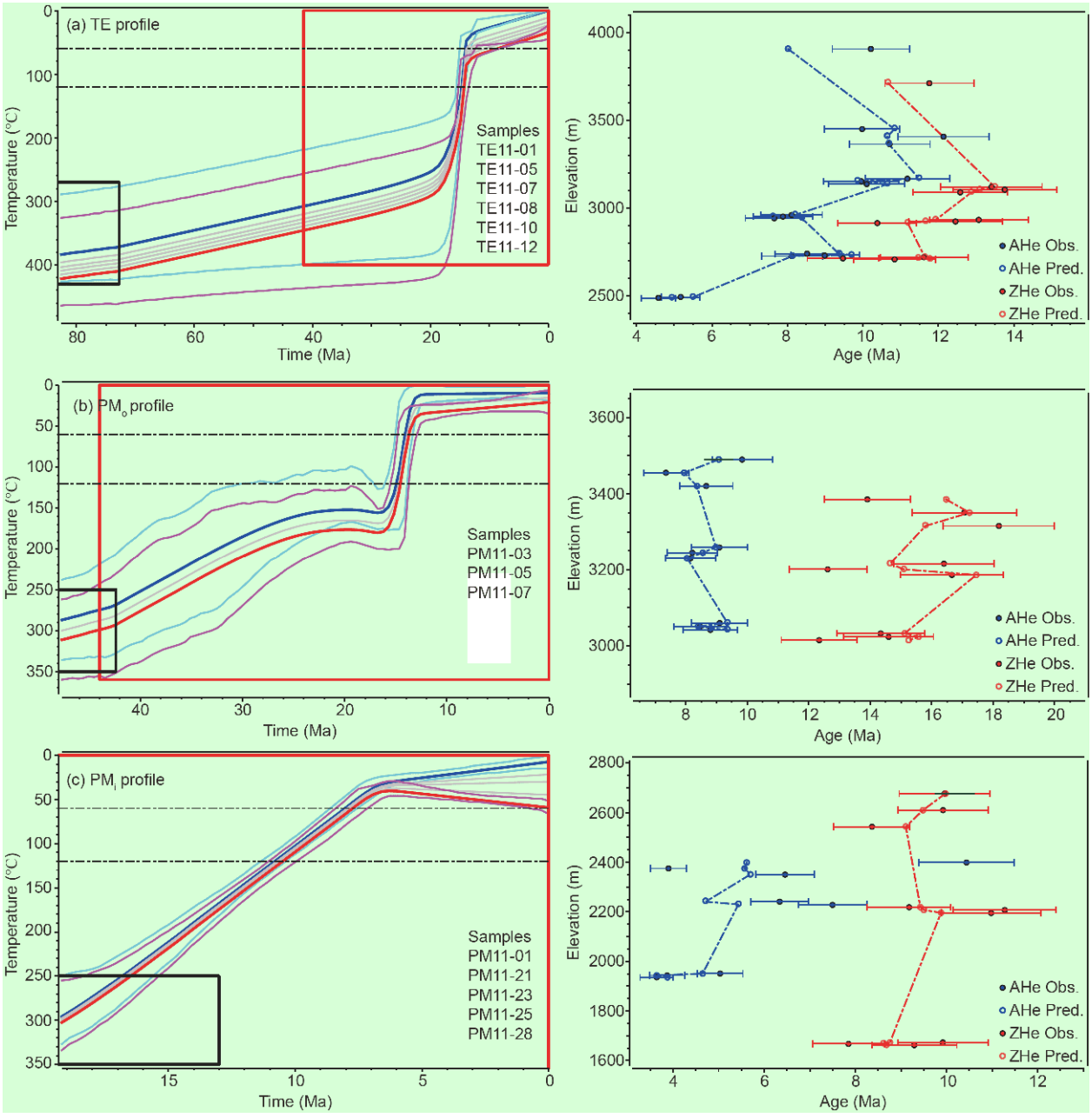

Figure 8 Thermal history QTQt modeling result for PM and TE pseudo-vertical profiles. QTQt inverse modeling was based on ZHe and AHe data. The black solid boxes are initial constraints based on the biotite $^{40}Ar/^{39}Ar$ data. Blue line corresponds to the uppermost sample with the 95% confidence interval in cyan. The thermal history of the lowermost sample is shown in red, with the 95% confidence interval in magenta. Gray lines represent the middle samples.

A summary of the exhumation history based on the Pecube model results is presented in Figure 11, and it assumes a three-stage scenario for this profile. The starting time (T_1) of the Pecube model was set to 18 Ma based on the oldest ZHe age (17.2 Ma). This inversion set comprises 10800 forward models that converged towards a lowest misfit value of 3.6. T_1 is the starting time. T_2 and T_3 were solved with best fits of 11 Ma and 3–5 Ma, respectively. The corresponding exhumation rates are <0.22 km Myr^{-1} for the first stage (E_1); <0.06 km Myr^{-1} for the second stage (E_2); and 0.8–1.2 km Myr^{-1} for the third stage (E_3). However, E_1 is poorly constrained (Figure 11). The inverse modeling results suggest that the TE profile experienced a three-stage exhumation like as PM$_i$ profile, consisting of slight rapid exhumation (<0.2 km Myr^{-1}) during the interval of 18–11 Ma, followed by slow exhumation, and an order of magnitude increase in exhumation since 3.5 Ma. For the TE profile, an exhumation rate of 0.11–0.25 km Ma^{-1} is predicted for the time interval of ~15–11 Ma (Figure 10) according to the analytical method of Willett and Brandon (2013).

The modeling results for the ZHe and AHe data using QTQt are presented in Figure 8. The predicted best-fit

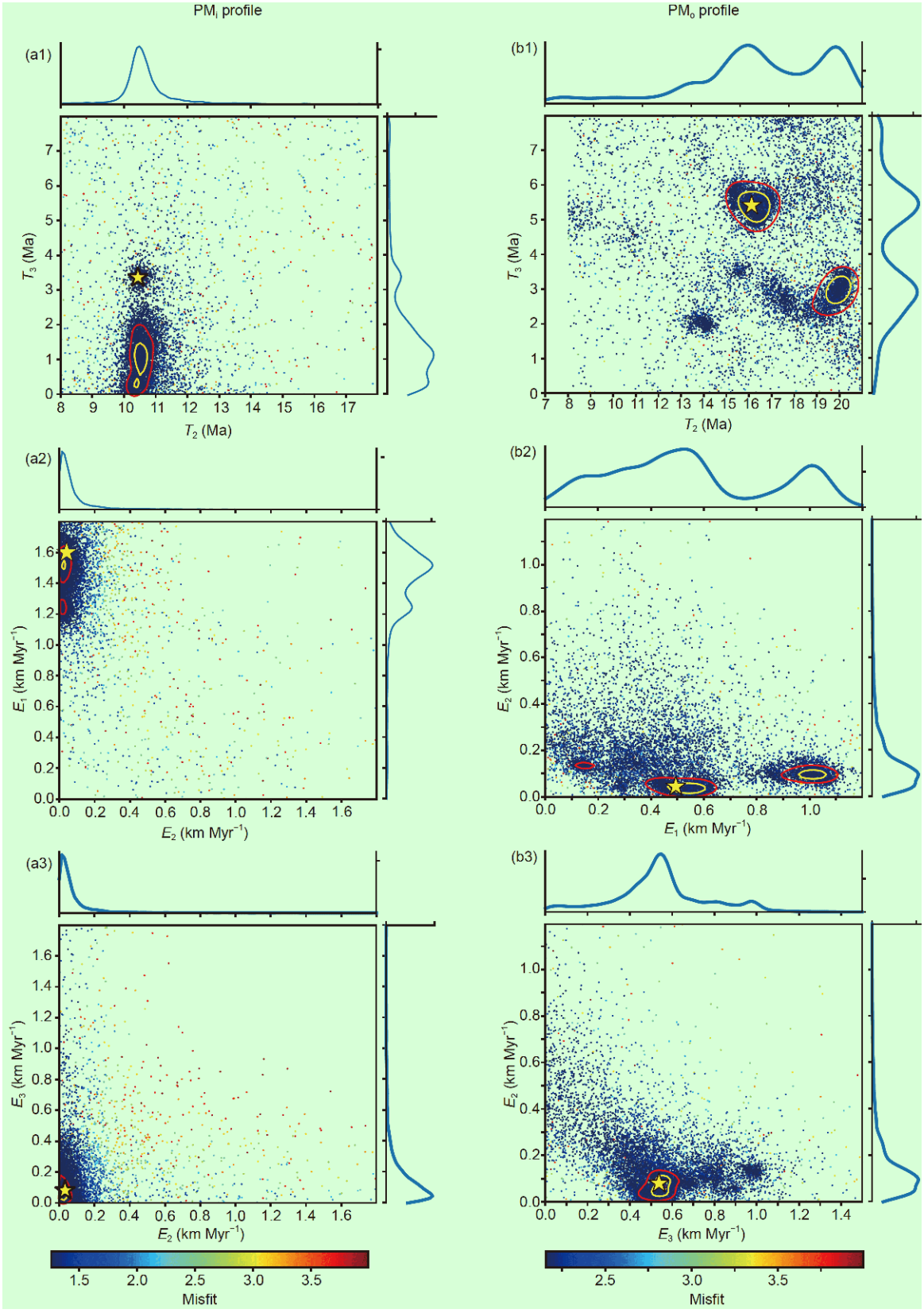

Figure 9 Pecube inversion results for PM$_i$ and PM$_o$ profiles from 3-D thermokinematic modelling using Pecube, shown as 2D scatter plots of inversion results and 1D posterior probability-density functions (PDFs) of parameter values. Each point represents one individual forward model, colored by misfit value. The optimal solution is shown by a star. T_2: onset of transition time of the second exhumation phase; T_3: the onset of transition time of third exhumation phase. E_1: the exhumation rates of the first phase; E_2: the exhumation rate of the second phase; E_3: the exhumation rate of the third phases.

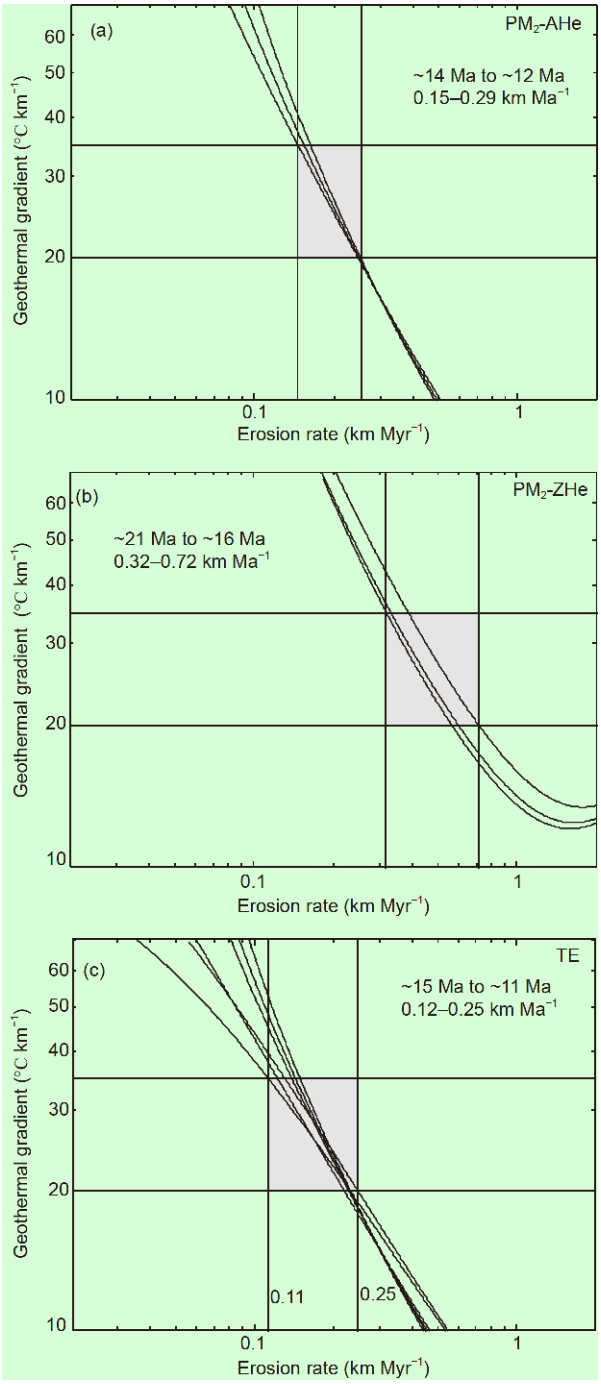

Figure 10 (a) and (b) show the erosion rate modeling for the AHe and ZHe data from PM_o profile. An erosional rate of 0.32–0.72 km Myr^{-1} using ZHe data is predicted for the time interval from ca. 21 to ca. 16 Ma. The predicted erosion rate using AHe data is 0.15–0.25 km Myr^{-1} between ca. 14 to ca.12 Ma. Model TE profile (c), an erosional rate of 0.11–0.25 km Ma^{-1} is predicted for the time interval from ca. 15 to ca. 11 Ma. The age of the lowest sample is used as the starting time of each time interval, as illustrated by Willett and Brandon (2013).

cooling curves for the TE profile show a three-stage cooling history (Figure 8). The first stage of cooling before 18 Ma was slow, but the rocks experienced extremely rapid cooling of <30°C Myr^{-1} during the interval of 18–13 Ma, followed by slowing cooling at a rate of <5°C Myr^{-1} (Figure 8). The QTQt model results for the TE profile show a similar cooling history to profile PM_i after 18 Ma. However, this late-stage (<13 Ma) slow cooling is not consistent with the He data for the same area. Previous workers reported the AHe and ZHe ages of <5 Ma from the riverbed (Wang et al., 2008; Yang et al., 2016; Wang et al., 2018) suggesting that rapid exhumation (>3 km) after ~5 Ma. Our QTQt model probably overpredicted the cooling rate during the interval of 18–13 Ma and did not provide information about the phase of rapid exhumation after ~5 Ma. Therefore, the QTQt modeling results are not consistent with the evidence of the low-temperature thermochronological data in this study and do not provide reliable information about thecooling history.

The results also show that the exhumation histories of the shear zone (PM_i profile) are substantially different from that of the area outside the shear zone (PM_o and TE profile, Figure 12). During the interval of 18–11 Ma, the shear zone experienced higher exhumation than that of the area outside, but after 11 Ma the entire area experienced a consistent two-stage exhumation history.

6. Discussion

6.1 Tectonic cooling and exhumation associated with shearing

Our results suggest a large difference in exhumation rate between the interior of the shear zone and the area outside before ~11 Ma. The cooling rate inside the shear zone was much greater than that outside during the interval of 18–11 Ma. According to the new zircon U-Pb ages, biotite $^{40}Ar/^{39}Ar$ ages, and field observations, the PM_o and TE profiles are located outside the Gaoligong and Chongshan shear zones, respectively, whereas the PM_i profile is within the Gaoligong shear zone. The Pecube modeling results of the PM_o and TE profiles (outside the shear zone) indicate a similar relatively slow cooling history before ~11 Ma. On the other hand, the exhumation history of the PM_i profile (inside the Gaoligong shear zone) indicates an episode of very rapid exhumation (~1.2 km Myr^{-1}) before 11 Ma (Figure 12). However, after ~11 Ma, the exhumation rates are similar for areas inside and outside the Gaoligong shear zone, with slow and quiescent exhumation during the interval of 11–5 Ma, and accelerated exhumation after ~5 Ma.

There may be several reasons for the variation in exhumation rate between samples within and outside the shear zone before 11 Ma. First, the most important reason is the differences in thermodynamic processes. Deformation-related processes in the shear zone, such as dynamic recrystallization, neocrystallization and fluid circulation, have been shown to be crucial for the interpretation of low-temperature thermochronological data (Lacassin et al., 1996;

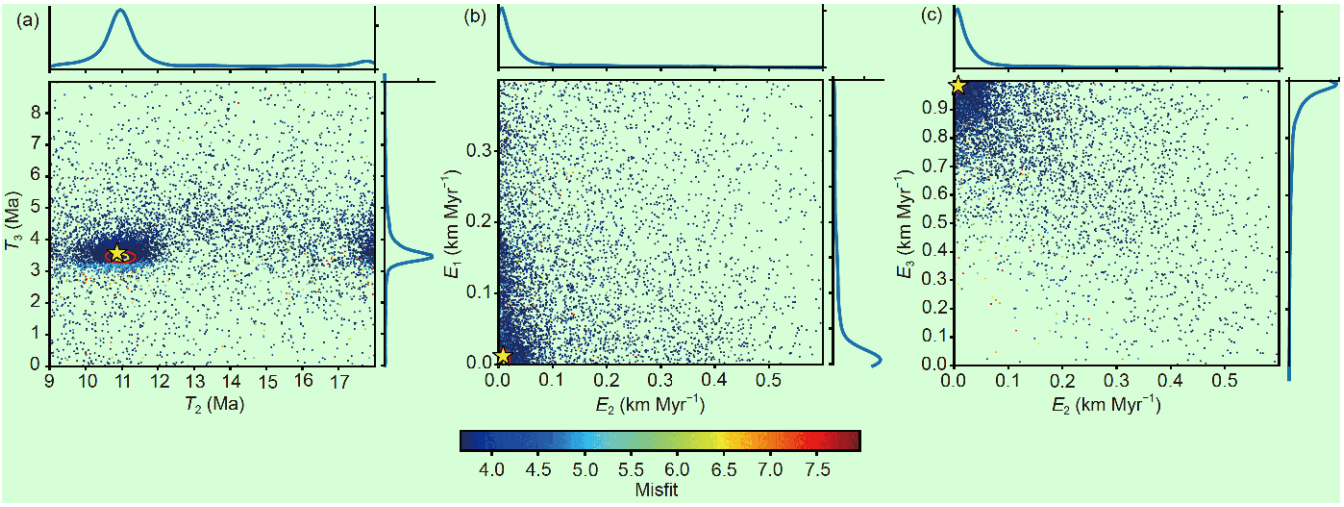

Figure 11 Pecube inversion results for TE profile from 3-D thermokinematic modelling using Pecube, shown as 2D scatter plots of inversion results and 1D posterior probability-density functions (PDFs) of parameter values. Each point represents one individual forward model, colored by misfit value. The optimal solution is shown by a star. T_2: onset of transition time of the second exhumation phase; T_3: the onset of third exhumation phase. E_1: the exhumation rates of the first phase; E_2: the exhumation rate of the second phase; E_3: the exhumation rate of the third phases.

Oriolo et al., 2018). The zircon U-Pb ages and biotite ^{40}Ar/^{39}Ar ages from inside the shear zone are much younger than those from outside. Within the PM profile, both the zircon U-Pb ages and biotite ^{40}Ar/^{39}Ar ages from outside the shear zone are older than 48 Ma, while the biotite ^{40}Ar/^{39}Ar ages are ~18 Ma (Lin et al., 2009, Figure 3). Petrographic observations and P-T paths reveal that the Gaoligong shear zone experienced an early stage of amphibolite facies metamorphism, followed by green schist facies and retrograde metamorphism during the late stage (Song et al., 2010; Zhang et al., 2012b, 2012a). The non-mylonitic leucogranite intrusions within the shear zone are interpreted to be produced by partial crustal melting during shearing before 18 Ma (Akciz et al., 2003; Song et al., 2010). Akciz et al. (2004) suggested that strike-slip shearing along the Gaoligong shear zone terminated before ~18 Ma, based on U-Pb ages of monazite grains from deformed and foliation cross-cutting leucogranites. This suggests that the shear zones have experienced rapid cooling from peak metamorphism before or around ~18 Ma.

The Gaoligong shear zone is a long and narrow metamorphic belt with strongly developed mylonitic textures. The geometry and deformation intensity of the shear zone suggest that the intensity of deformation decreases from the center to both sides, especially to the western side (Huang et al., 2015). Song et al. (2010) proposed a late-stage metamorphism of the greenschist facies after the early Miocene, which suggests that deformation before the early Miocene was mostly localized within shear zones. For this reason, geochronological data from the shear zones may record not only the exhumation, but also the influence by neo- or recrystallization, fluid-assisted deformation and inheritance of the protolith age. After 18 Ma, the shear zone cooled to below 350°C, based on the biotite ^{40}Ar/^{39}Ar ages. This phase of rapid cooling was probably caused by a decrease of the shearing. The ZHe and AHe ages show a positive age-elevation correlation after 18 Ma in the shear zone (Figure 3), suggesting a cooling phase probably generated by regional relaxation of thermal gradients, or by the advection of rock towards the surface (e.g. Ring et al., 1999; Reiners and Brandon, 2006). Thus, the early Miocene rapid cooling pattern of the PM$_i$ profile that we have determined may be restricted to the shear zones as a result of thermal perturbations caused by the activity of the shear zones, rather than being caused by rapid exhumation or uplift.

Although our results indicate that the activity of the shear zone may have begun to weaken at 18 Ma, the exact termination of the shearing is not well constrained. Wang et al. (2018) suggested that the main phase of shearing occurred during the interval of 19–11 Ma, based on the interpretation of low-temperature thermochronological data; whereas Akciz et al. (2008) suggested that the shear zone was terminated by ~17 Ma, based on the ^{40}Ar/^{39}Argeochronological studies. We suggest that the termination or a slowing-down of the shearing along the Gaoligong shear zone probably occurred at ~11 Ma, based on a comparison of the exhumation history outside and inside the shear zone. When the shearing ceased or slowed down, the exhumation history would tend to be similar inside and outside the shear zone. Indeed, the apatite and zircon (U-Th)/He data and Pecube model results of the Pianma profiles reveal a similarly two-stage exhumation history for both inside and outside the Gaoligong shear zone: lower magnitude cooling during ~11–5 Ma, followed by a rapid and prominent cooling event after the early Pliocene (Figure 12). In addition, the ^{40}Ar/^{39}Ar ages of muscovite and biotite are within the range of 19–11 Ma (Akciz, 2004; Wang

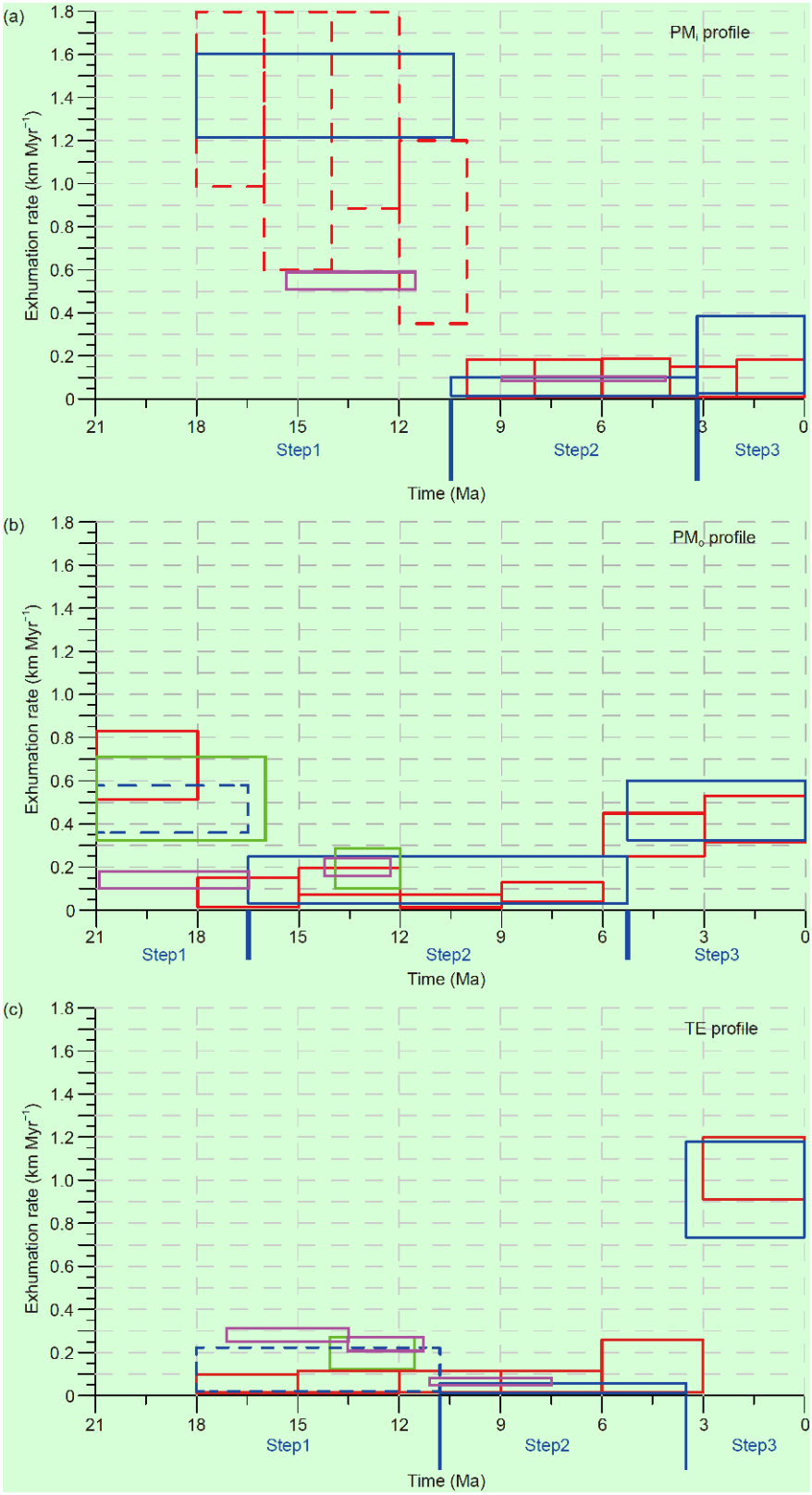

Figure 12 Modeling scenarios of the exhumation rates over time using the three-dimensional numerical thermal-kinematic code Pecube (Braun et al., 2012) for (a) PM_i, (b) PM_o, and (c) TE profiles. Shown in red, the exhumation rates at 2 Ma-interval for PM_i, 3 Ma-interval for PM_o, and 3 Ma-interval for TE profiles are calculated for detecting possible exhumation transition node. The history shown in blue is the modeling of three-phase scenario with searching for the best solutions of onset timing and exhumation rate, guided by the 2–3 Ma-interval modeling results (in red line) and AER of the thermochronologic data. The parameters for the models are in Table S1. Dotted lines mean a bit poor concentrated results. The green squares mean exhumation rates calculated by the method of Willett and Brandon (2013). The Fuchsia squares mean exhumation rates calculated by age-elevation relationship method.

et al., 2006; Lin et al., 2009; Zhang et al., 2012b, 2012a), which can be interpreted as the result of mica growth during shearing, and thus may represent the minimum age of the shearing event (Akciz et al., 2008).

6.2 Regional pattern and control of exhumation

Despite the fact that prior to ~11 Ma the cooling rate of the internal shear zone was different to that outside the shear zone, the temporal change in cooling appears to be synchronous, which defines four stages: before 18 Ma, 18–11 Ma, 10–5 Ma, and after ~5 Ma.

The internal temperature of the Gaoligong shear zone shear zone remained high until ~18 Ma in the PM_i profile; subsequently, the rocks within the shear zone cooled to below ~350°C, as recorded by $^{40}Ar/^{39}Ar$ ages (Lin et al., 2009). The Pecube result for the profile PM_o shows that the exhumation rate was 0.4–0.6 km Myr^{-1} during the interval of 21–17 Ma outside the shear zone, which is greater than that during the interval of 17–5 Ma (0.05–0.19 km Myr^{-1}). Although the thermal cooling rate in the shear zone was faster after ~18 Ma, based on the low-temperature thermochronological data, it is impossible to confirm whether the cooling rate suddenly accelerated at ~18 Ma. Therefore, low-temperature thermochronological data cannot provide robust constraints on the cooling history before 18 Ma.

Comparison of the exhumation rates inside and outside the shear zones shows that the tectonic-induced exhumation or cooling during the interval of 18–11 Ma was mainly localized in the shear zones. Barring the possibility of a tectonic origin, Nie et al. (2018) interpreted the mid-Miocene fast exhumation at ~300 km south of our TE profile and downstream along the Mekong River as being caused by high monsoon precipitation during the period. However, our detailed thermochronology data indicate that the mid-Miocene phase of enhanced fast cooling occurred mainly in the interior of the shear zones, indicating that tectonic forces should not be ignored along the rivers. During the same period, the area outside the shear zone (PM_o and TE profile, Figure 12) in the river valleys experienced slow exhumation, which cannot be explained by intensified monsoon precipitation. The rapid cooling within shear zones may be associated with the exhumation and localized relaxation of thermal gradients at this time, rather than resulting solely from climate driven exhumation and cooling. Moreover, both our results and those of Wang et al. (2018) suggest that the episode of rapid exhumation was during 18–11 Ma, which includes but continued beyond the period of 17–14 Ma with intensified monsoon precipitation proposed by Nie et al. (2018). Low-temperature thermochronological data are very sensitive to tectonic activity and fluvial incision, and either factor can substantially increase the exhumation rate. The low-temperature thermochronological ages in the shear zone or valleys are substantially younger than those in the exterior area (Safran et al., 2006; Zhang et al., 2016; Schildgen et al., 2018). However, there is no large gap in ZHe or AHe data between inside and outside of the shear zone (Figure 3). This likely indicates that the shearing did not have much influence on exhumation, and the rapid cooling implies the weakness of shearing, rather than the reinforcement of shearing, during 18–11 Ma.

The internal and external areas of the shear zone underwent consistent exhumation after 11 Ma. The termination or weakening of the shearing effect was likely the main reason for the abrupt slowing of the exhumation rate after 11 Ma, especially within the interior of the shear zone (Figure 12). The youngest group of $^{40}Ar/^{39}Ar$ ages of weakly-deformed leucogranite and protomylonite are ~11 Ma, suggesting that the shearing probably ceased at that time (Akciz, 2004; Lin et al., 2009; Zhang et al., 2009). The Gaoligong shear zone was reported as dextral shearing under amphibolite facies to greenschist facies metamorphism by ~11 Ma (Xu et al., 2015). The $^{40}Ar/^{39}Ar$ ages from these greenschist facies orthogneiss samples may correspond to the time of mica growth during shearing, and thus they may represent the minimum age of the shearing event (Akciz et al., 2008). In addition, there was no large difference in the rate of exhumation inside and outside the shear zone after 11 Ma (Figure 12), indicating that the shearing subsequently had little influence on exhumation.

Our data suggest that the exhumation rate suddenly increased since 3–5 Ma, following a period of slow cooling which lasted for ~6 Myrs, along the Langcang-Mekong River and Nu Jiang-Salween River at latitude ~26°N. We suggest that a combination of regional extension and climate change since the late Miocene-Pliocene contributed to the observed rapid cooling in the southeastern Tibetan Plateau. In many locations along the Mekong and Salween rivers, the youngest AHe or ZHe ages are less than 5 Ma along the riverbeds (Wang et al., 2008; Yang et al., 2016; Liu-Zeng et al., 2018; Wang et al., 2018). This means that the region should have experienced an exhumation of more than 2–4 km after ~5 Ma. Based on longitudinal profiles of tributaries and low-temperature thermorchoronological data, previous studies attributed this phase of fast exhumation to increased fluvial incision (Yang et al., 2016; Wang et al., 2018). It is tempting to attribute to Pliocene-Pleistocene climate cooling for elevated incision (Herman et al., 2013). However, it is difficult to rule out the possibility that regional EW extension was contributed to the rapid exhumation in the southern borderland of Tibet. Regional extension would cause an increase in relative relief either regionally or locally, driving river incision. NE-NNE-trending rift basins and NS-striking normal faults are ubiquitous, which are characterized by transtensional dextral strike-slip (Socquet and Pubellier, 2005; Wang et al., 2007).

Petrological and geochemical evidence and thermal-mechanical modeling results suggest that the upwelling of the asthenosphere may provide the heat flow environment and the uplift to drive regionally widespread enhanced river incision in the southeastern Tibetan Plateau. More data are needed in a variety of different tectonic setting and geographic locations to distinguish the relative contribution of climate and tectonics.

7. Conclusion

New zircon U-Pb, biotite $^{40}Ar/^{39}Ar$, and apatite and zircon (U-Th)/He thermochronometry analyses in the Pianma and Tu'er areas indicate that the lower Pianma profile, located inside the Gaoligong shear zone, experienced an episode of very rapid exhumation (~1.2 km Myr^{-1}) during the interval of 18–11 Ma, a sharp decrease to <0.1 km Myr^{-1} during the interval of 11–3 Ma, and then a slight increase to <0.4 km Myr^{-1} after ~3 Ma. However, the upper Pianma profile, to the west of and outside the Gaoligong shear zone, exhibits a distinct three-stage exhumation history: an episode of rapid exhumation (<0.8 km Myr^{-1}) during the interval of 21–17 Ma, slow exhumation during the interval of 17–5 Ma, and an episode of rapid exhumation after ~5 Ma. Similar to the upper Pianma profile after 18 Ma, the Tu'er profile, to the east of the Chongshan shear zone, indicates a two-stage exhumation history: relatively slow exhumation during the interval of 18–4 Ma (<0.2 km Myr^{-1}), and rapid exhumation after ~4 Ma (>0.75 km Myr^{-1}). The exhumation history of inside the shear zone differs from that of outside the shear zone prior to ~11 Ma. Rapid exhumation during the interval of 18–11 Ma appears to have been restricted to the shear zone, which we attribute to exhumation and localized shearing-related cooling. After 11 Ma, both the areas within and outside the shear zone experienced a consistent two-stage exhumation history: slower cooling until the early Pliocene, and then a rapid increase in cooling since the early Pliocene, which probably means that the shearing weakened by ~11 Ma. The most recent pulse of rapid cooling since the early Pliocene was related to climate change or possibly to a transformation of the tectonic setting, leading to a transient acceleration of fluvial incision and the exhumation rate. There was substantial spatial variability of the degree of exhumation, but exhumation occurred simultaneously across the region, and this highlights the importance of the structural context in interpreting thermochronological data.

Acknowledgements *The manuscript benefits from constructive reviews by Zhang Bo, and anonymous reviewers. This work was supported by the National Natural Science Foundation of China (Grant Nos. 41761144065, 41902213 and 41702223), the State Key Laboratory of Earthquake Dynamics of China (Grant No. LED2016A02), the National Key Research and Development Project of China (Grant No. 2016YFC0600310), and the Natural Environment Research Council of UK (Grant No. NE/N015479/1).*

References

Akciz S. 2004. Structure and geochronological constraints on the ductile deformation observed along the Gaoligong Shan and Chong Shan Shear Zones, Yunnan (China). Dissertation for Doctoral Degree. Cambridge: Massachusetts Institute of Technology

Akciz S O, Burchfiel C B, Crowley J L, Jiyun Y, Liangzhong C. 2003. Gaoligong and Chong Shan shear zones, Yunnan, and accommodation of the northward movement of India relative to Indochina during the Mid-Cenozoic. AGU Fall Meeting Abstracts

Akciz S, Burchfiel B C, Crowley J L, Yin J Y, Chen L Z. 2008. Geometry, kinematics, and regional significance of the Chong Shan shear zone, Eastern Himalayan Syntaxis, Yunnan, China. Geosphere, 4: 292–314

Arne D, Worley B, Wilson C, Chen S F, Foster D, Luo Z L, Liu S G, Dirks P. 1997. Differential exhumation in response to episodic thrusting along the eastern margin of the Tibetan Plateau. Tectonophysics, 280: 239–256

Bermúdez M A, van der Beek P, Bernet M. 2011. Asynchronous Miocene-Pliocene exhumation of the central Venezuelan Andes. Geology, 39: 139–142

Blackburn T, Ferrier K L, Perron J T. 2018. Coupled feedbacks between mountain erosion rate, elevation, crustal temperature, and density. Earth Planet Sci Lett, 498: 377–386

Braun J. 2002. Estimating exhumation rate and relief evolution by spectral analysis of age-elevation datasets. Terra Nova, 14: 210–214

Braun J, van der Beek P, Valla P, Robert X, Herman F, Glotzbach C, Pedersen V, Perry C, Simon-Labric T, Prigent C. 2012. Quantifying rates of landscape evolution and tectonic processes by thermochronology and numerical modeling of crustal heat transport using PECUBE. Tectonophysics, 524-525: 1–28

Brookfield M E. 1998. The evolution of the great river systems of southern Asia during the Cenozoic India-Asia collision: Rivers draining southwards. Geomorphology, 22: 285–312

Burchfiel B C, Chen Z. 2013. Tectonics of the Southeastern Tibetan Plateau and its Adjacent Foreland. Boulder: Geological Society of America. 78–96

Bureau of Geology and Mineral Resources of Yunnan Province. 1990. Regional Geology of Yunnan Province. Beijing: Geological Publishing House. 115–168

Clark M K, House M A, Royden L H, Whipple K X, Burchfiel B C, Zhang X, Tang W. 2005. Late Cenozoic uplift of southeastern Tibet. Geology, 33: 525–528

Clark M K, Royden L H, Whipple K X, Burchfiel B C, Zhang X, Tang W. 2006. Use of a regional, relict landscape to measure vertical deformation of the eastern Tibetan Plateau. J Geophys Res, 111: 23

Dahlen F A, Suppe J. 1988. Mechanics, growth, and erosion of mountain belts. In: Clark S P, Jr Burchfiel B C, Suppe J, eds. Processes in Continental Lithospheric Deformation. Boulder: Geological Society of America. 161–178

Eroğlu S, Siebel W, Danišík M, Pfänder J A, Chen F. 2013. Multi-system geochronological and isotopic constraints on age and evolution of the Gaoligongshan metamorphic belt and shear zone system in western Yunnan, China. J Asian Earth Sci, 73: 218–239

Farley K A, Wolf R A, Silver L T. 1996. The effects of long alpha-stopping distances on (U-Th)/He ages. Geochim Cosmochim Acta, 60: 4223–4229

Fielding E, Isacks B, Barazangi M, Duncan C. 1994. How flat is Tibet? Geology, 22: 163–167

Fitzgerald P G, Muñoz J A, Coney P J, Baldwin S L. 1999. Asymmetric exhumation across the Pyrenean orogen: Implications for the tectonic evolution of a collisional orogen. Earth Planet Sci Lett, 173: 157–170

Flowers R M, Ketcham R A, Shuster D L, Farley K A. 2009. Apatite (U-Th)/He thermochronometry using a radiation damage accumulation and

annealing model. Geochim Cosmochim Acta, 73: 2347–2365
Gallagher K. 2012. Transdimensional inverse thermal history modeling for quantitative thermochronology. J Geophys Res, 117: 16
Gallagher K, Stephenson J, Brown R, Holmes C, Fitzgerald P. 2005. Low temperature thermochronology and modeling strategies for multiple samples 1: Vertical profiles. Earth Planet Sci Lett, 237: 193–208
Guenthner W R, Reiners P W, Ketcham R A, Nasdala L, Giester G. 2013. Helium diffusion in natural zircon: Radiation damage, anisotropy, and the interpretation of zircon (U-Th)/He thermochronology. Am J Sci, 313: 145–198
Hallet B, Molnar P. 2001. Distorted drainage basins as markers of crustal strain east of the Himalaya. J Geophys Res, 106: 13697–13709
Herman F, Seward D, Valla P G, Carter A, Kohn B, Willett S D, Ehlers T A. 2013. Worldwide acceleration of mountain erosion under a cooling climate. Nature, 504: 423–426
Hou K, Li Y, Tian Y. 2009. In situ U-Pb zircon dating using laser ablation-multion counting-ICP-MS (in Chinese). Miner Depos, 28: 481–492
Huang X M, Xu Z Q, Li H Q, Cai Z H. 2015. Tectonic amalgamation of the Gaoligong shear zone and Lancangjiang shear zone, southeast of Eastern Himalayan Syntaxis. J Asian Earth Sci, 106: 64–78
Ji J, Zhong D L, Zhang L S. 2000. Kinematics and dating of Cenozoic strike-slip faults in the Tengchong area, west Yunnan: Implications for the block movement in the southeastern Tibet Plateau (in Chinese). Sci Geol Sin, 35: 336–349
Jolivet L, Beyssac O, Goffé B, Avigad D, Lepvrier C, Maluski H, Thang T T. 2001. Oligo-Miocene midcrustal subhorizontal shear zone in Indochina. Tectonics, 20: 46–57
Lacassin R, Schärer U, Leloup P H, Arnaud N, Tapponnier P, Liu X, Zhang L. 1996. Tertiary deformation and metamorphism SE of Tibet: The folded Tiger-leap décollement of NW Yunnan, China. Tectonics, 15: 605–622
Leloup P H, Arnaud N, Lacassin R, Kienast J R, Harrison T M, Trong T T P, Replumaz A, Tapponnier P. 2001. New constraints on the structure, thermochronology, and timing of the Ailao Shan-Red River shear zone, SE Asia. J Geophys Res, 106: 6683–6732
Leloup P H, Harrison T M, Ryerson F J, Chen W, Li Q, Tapponnier P, Lacassin R. 1993. Structural, petrological and thermal evolution of a Tertiary ductile strike-slip shear zone, Diancang Shan, Yunnan. J Geophys Res, 98: 6715–6743
Leloup P H, Lacassin R, Tapponnier P, Schärer U, Zhong D, Liu X, Zhang L, Ji S, Trinh P T. 1995. The Ailao Shan-Red River shear zone (Yunnan, China), Tertiary transform boundary of Indochina. Tectonophysics, 251: 3–84
Lin T H, Lo C H, Chung S L, Hsu F J, Yeh M W, Lee T Y, Ji J Q, Wang Y Z, Liu D. 2009. $^{40}Ar/^{39}Ar$ dating of the Jiali and Gaoligong shear zones: Implications for crustal deformation around the Eastern Himalayan Syntaxis. J Asian Earth Sci, 34: 674–685
Liu-Zeng J, Zhang J Y, McPhillips D, Reiners P, Wei W, Pik R, Zeng L S, Hoke G, Xie K J, Ping X, Zheng D W, Ge Y K. 2018. Multiple episodes of fast exhumation since Cretaceous in southeast Tibet, revealed by low-temperature thermochronology. Earth Planet Sci Lett, 490: 62–76
Liu-Zeng J, Tapponnier P, Gaudemer Y, Ding L. 2008. Quantifying landscape differences across the Tibetan plateau: Implications for topographic relief evolution. J Geophys Res, 113: 26
Ludwig K R. 2003. ISOPLOT 3.00: A Geochronological Toolkit for Microsoft Excel. California: Berkeley Geochronology Center
Molnar P, England P, Martinod J. 1993. Mantle dynamics, uplift of the Tibetan Plateau, and the Indian Monsoon. Rev Geophys, 31: 357–396
Moore M A, England P C. 2001. On the inference of denudation rates from cooling ages of minerals. Earth Planet Sci Lett, 185: 265–284
Morley C K. 2007. Variations in Late Cenozoic-Recent strike-slip and oblique-extensional geometries, within Indochina: The influence of pre-existing fabrics. J Struct Geol, 29: 36–58
Nie J, Ruetenik G, Gallagher K, Hoke G, Garzione C N, Wang W, Stockli D, Hu X, Wang Z, Wang Y, Stevens T, Danišík M, Liu S. 2018. Rapid incision of the Mekong River in the middle Miocene linked to monsoonal precipitation. Nat Geosci, 11: 944–948
Oriolo S, Wemmer K, Oyhantçabal P, Fossen H, Schulz B, Siegesmund S. 2018. Geochronology of shear zones—A review. Earth-Sci Rev, 185: 665–683
Ouimet W, Whipple K, Royden L, Reiners P, Hodges K, Pringle M. 2010. Regional incision of the eastern margin of the Tibetan Plateau. Lithosphere, 2: 50–63
Reiners P W, Brandon M T. 2006. Using thermochronology to understand orogenic erosion. Annu Rev Earth Planet Sci, 34: 419–466
Ring U, Brandon M T, Willett S D, Lister G S. 1999. Exhumation processes. Geol Soc Lond Spec Publ, 154: 1–27
Royden L H, Burchfiel B C, van der Hilst R D. 2008. The geological evolution of the Tibetan Plateau. Science, 321: 1054–1058
Safran E B, Blythe A, Dunne T. 2006. Spatially variable exhumation rates in orogenic belts: An Andean example. J Geol, 114: 665–681
Sang H Q, Wang S S, Qiu J. 1996. The $^{40}Ar/^{39}Ar$ ages of pyroxene, hornblende and plagioclase in Taipingzhai granulites in Qianxi County, Hebei Province and their geological implications (in Chinese with English abstract). Acta Petr Sin, 12: 390–400
Schärer U, Tapponnier P, Lacassin R, Leloup P H, Zhong D, Ji S. 1990. Intraplate tectonics in Asia: A precise age for large-scale Miocene movement along the Ailao Shan-Red River shear zone, China. Earth Planet Sci Lett, 97: 65–77
Schildgen T F, van der Beek P A, Sinclair H D, Thiede R C. 2018. Spatial correlation bias in late-Cenozoic erosion histories derived from thermochronology. Nature, 559: 89–93
Shen X, Tian Y, Li D, Qin S, Vermeesch P, Schwanethal J. 2016. Oligocene-Early Miocene river incision near the first bend of the Yangze River: Insights from apatite (U-Th-Sm)/He thermochronology. Tectonophysics, 687: 223–231
Socquet A, Pubellier M. 2005. Cenozoic deformation in western Yunnan (China-Myanmar border). J Asian Earth Sci, 24: 495–515
Song S, Niu Y, Wei C, Ji J, Su L. 2010. Metamorphism, anatexis, zircon ages and tectonic evolution of the Gongshan block in the northern Indochina continent—An eastern extension of the Lhasa Block. Lithos, 120: 327–346
Tapponnier P, Lacassin R, Leloup P H, Schärer U, Zhong D, Wu H, Liu X, Ji S, Zhang L, Zhong J. 1990. The Ailao Shan/Red River metamorphic belt: Tertiary left-lateral shear between Indochina and South China. Nature, 343: 431–437
Tian Y T, Li R, Tang Y, Xu X, Wang Y J, Zhang P Z. 2018. Thermochronological constraints on the late Cenozoic morphotectonic evolution of the Min Shan, the eastern margin of the Tibetan Plateau. Tectonics, 37: 1733–1749
Tian Y T, Kohn B P, Gleadow A J W, Hu S B. 2014. A thermochronological perspective on the morphotectonic evolution of the southeastern Tibetan Plateau. J Geophys Res-Solid Earth, 119: 676–698
Wagner G A, Reimer G M. 1972. Fission track tectonics: The tectonic interpretation of fission track apatite ages. Earth Planet Sci Lett, 14: 263–268
Wang E, Burchfiel B C. 1997. Interpretation of Cenozoic tectonics in the right-lateral accommodation zone between the Ailao Shan shear zone and the eastern Himalayan syntaxis. Int Geol Rev, 39: 191–219
Wang E, Kirby E, Furlong K P, van Soest M, Xu G, Shi X, Kamp P J J, Hodges K V. 2012. Two-phase growth of high topography in eastern Tibet during the Cenozoic. Nat Geosci, 5: 640–645
Wang G, Wan J L, Wang E C, Zheng D W, Li F. 2008. Late Cenozoic to recent transtensional deformation across the southern part of the Gaoligong shear zone between the Indian plate and SE margin of the Tibetan plateau and its tectonic origin. Tectonophysics, 460: 1–20
Wang H, Tian Y, Liang M. 2017. Late Cenozoic exhumation history of the Luoji Shan in the southeastern Tibetan Plateau: Insights from apatite fission-track thermochronology. J Geol Soc, 174: 883–891
Wang Y, Fan W, Zhang Y, Peng T, Chen X, Xu Y. 2006. Kinematics and $^{40}Ar/^{39}Ar$ geochronology of the Gaoligong and Chongshan shear systems, western Yunnan, China: Implications for early Oligocene tectonic extrusion of SE Asia. Tectonophysics, 418: 235–254
Wang Y, Zhang B, Schoenbohm L M, Zhang J J, Zhou R, Hou J, Ai S. 2016. Late Cenozoic tectonic evolution of the Ailao Shan-Red River

fault (SE Tibet): Implications for kinematic change during plateau growth. Tectonics, 35: 1969–1988
Wang Y, Zhang X, Jiang C, Wei H, Wan J. 2007. Tectonic controls on the late Miocene-Holocene volcanic eruptions of the Tengchong volcanic field along the southeastern margin of the Tibetan plateau. J Asian Earth Sci, 30: 375–389
Wang Y, Zhang P Z, Schoenbohm L M, Zheng W J, Zhang B, Zhang J J, Zheng D W, Zhou R J, Tian Y T. 2018. Two-phase exhumation along major shear zones in the SE Tibetan Plateau in the late Cenozoic. Tectonics, 37: 2675–2694
Willett S D, Brandon M T. 2013. Some analytical methods for converting thermochronometric age to erosion rate. Geochem Geophys Geosyst, 14: 209–222
Wilson C J L, Fowler A P. 2011. Denudational response to surface uplift in east Tibet: Evidence from apatite fission-track thermochronology. Geol Soc Am Bull, 123: 1966–1987
Wolf R A, Farley K A, Silver L T. 1996. Helium diffusion and low-temperature thermochronometry of apatite. Geochim Cosmochim Acta, 60: 4231–4240
Wu F Y, Yang Y H, Xie L W, Yang J H, Xu P. 2006. Hf isotopic compositions of the standard zircons and baddeleyites used in U-Pb geochronology. Chem Geol, 234: 105–126
Xu Z Q, Wang Q, Cai Z H, Dong H W, Li H Q, Chen X J, Duan X D, Cao H, Li J, Burg J P. 2015. Kinematics of the Tengchong Terrane in SE Tibet from the late Eocene to early Miocene: Insights from coeval mid-crustal detachments and strike-slip shear zones. Tectonophysics, 665: 127–148
Yang R, Fellin M G, Herman F, Willett S D, Wang W, Maden C. 2016. Spatial and temporal pattern of erosion in the Three Rivers Region, southeastern Tibet. Earth Planet Sci Lett, 433: 10–20
Zhang B, Zhang J J, Zhong D L, Guo L. 2009. Strain and kinematic vorticity analysis: An indicator for sinistral transpressional strain-partitioning along the Lancangjiang shear zone, western Yunnan, China. Sci China Ser D-Earth Sci, 52: 602–618
Zhang B, Zhang J, Chang Z, Wang X, Cai F, Lai Q. 2012b. The Biluoxueshan transpressive deformation zone monitored by synkinematic plutons, around the Eastern Himalayan Syntaxis. Tectonophysics, 574-575: 158–180
Zhang B, Zhang J, Zhong D. 2010. Structure, kinematics and ages of transpression during strain-partitioning in the Chongshan shear zone, western Yunnan, China. J Struct Geol, 32: 445–463
Zhang B, Zhang J J, Zhong D L, Wang X X, Qu J F, Guo L. 2011. Structural feature and its significance of the northernmost segment of the Tertiary Biluoxueshan-Chongshan shear zone, east of the Eastern Himalayan Syntaxis. Sci China Earth Sci, 54: 959–974
Zhang B, Zhang J, Zhong D, Yang L, Yue Y, Yan S. 2012a. Polystage deformation of the Gaoligong metamorphic zone: Structures, $^{40}Ar/^{39}Ar$ mica ages, and tectonic implications. J Struct Geol, 37: 1–18
Zhang H, Oskin M E, Liu-Zeng J, Zhang P, Reiners P W, Xiao P. 2016. Pulsed exhumation of interior eastern Tibet: Implications for relief generation mechanisms and the origin of high-elevation planation surfaces. Earth Planet Sci Lett, 449: 176–185
Zhang J Y, Liu-Zeng J, Scherler D, Yin A, Wang W, Tang M Y, Li Z F. 2018. Spatiotemporal variation of late Quaternary river incision rates in southeast Tibet, constrained by dating fluvial terraces. Lithosphere, 10: 662–675
Zhong D, Tapponnier P, Wu H W, Zhang L S, Ji S, Zhong J Y, Liu X H, Schärer U, Lacassin R, Leloup P H. 1990. Large-scale strike-slip-fault-the major structure of intracontinental deformation after collision. Chin Sci Bull, 35: 304–304

(Responsible editor: Shaofeng LIU)